

國立交通大學  
材料科學與工程學系  
博士論文

鐵錳鋁鉻碳合金相變化與抗腐蝕



研究生：段逸軒

指導教授：劉增豐 博士

朝春光 博士

中華民國九十九年七月

# Phase Transformations and Corrosion Behaviors in Fe-Mn-Al-Cr-C Alloys

研究生：段逸軒

Student: Yi-Hsuan Tuan

指導教授：劉增豐 博士

Advisor: Prof. Tzeng-Feng Liu

朝春光 博士

Prof. Chuen-Guang Chao

國立交通大學

材料科學與工程學系

博士論文

A Dissertation

Submitted to Department of Materials Science and Engineering

College of Engineering

National Chiao Tung University

in Partial Fulfillment of the Requirements

for the Degree of

Doctor of Philosophy

in

Materials Science and Engineering

July 2010

Hsinchu, Taiwan, Republic of China

中華民國九十九年七月

## 致謝

由衷的感謝指導老師劉增豐教授以及朝春光教授多年來的悉心指導以及諄諄教誨，使學生的研究實驗能夠順利且完成此論文。除了在研究領域上所遇到的困難之外，劉增豐教授對學生在生活上所遇到的問題與困難，也總是時時的關心以及開導，對於學生能夠持續不放棄的完成學業有莫大的影響，對此心中也是十二萬分的感激。另外也要感謝師母林美慧老師多年來對學生的關心以及鼓勵，學生僅此致上最誠摯的感謝。

感謝實驗室的眾多學長學弟們在實驗過程及論文撰寫中對我的幫助。學長鄭祥成博士、李堅瑋博士、陳志壕博士、王承舜博士、楊勝裕博士、學弟蘇俊瑋博士，對於我在儀器的使用操作及分析上，給予了無私的教導與幫助。另外蔡國棟學長、學弟志龍、伯至、浩仰、凱明、永昌、信良以及眾多曾經共事過的同學及學弟們，對於我在生活及論文撰寫上也給予了很大的幫助，對此由衷的表示感謝。也希望還在為了各自的學位及將來奮鬥的學弟們，在接下來的日子裡，不論在學業上或是在生活上都能一切順心。

最後我最需要感謝的就是我最親愛的父母、家人以及總是在背後默默支持我的另一半其芬，有了你們多年來的支持以及鼓勵，我才能夠心無旁騖、無後顧之憂的完成我的學業。對於你們的付出，我的心中只有滿滿的感恩與感動。

# 鐵錳鋁鉻碳合金相變化與抗腐蝕

研究生：段逸軒

指導教授：劉增豐 博士

朝春光 博士

國立交通大學材料科學與工程學系

## 中文摘要

本論文利用掃描式電子顯微鏡，穿透式電子顯微鏡與 X 光能量散佈分析儀等，觀察研究單一沃斯田鐵以及(肥粒鐵 + 沃斯田鐵)雙相 FeMnAlCrC 合金之顯微結構及抗腐蝕性。依據實驗結果，本論文所得到的具體研究結果如下：

- (一)、在淬火狀態下，Fe-30wt.%Mn-9wt.%Al-5wt.%Cr-0.7wt.%C 合金的顯微結構為單一沃斯田鐵相。當此合金在 550 到 750°C 時效處理後，細微的  $(\text{Fe},\text{Mn})_3\text{AlC}$  碳化物 ( $k'$  碳化物) 會在沃斯田鐵相基地內形成。此外，隨著時效溫度的上昇，在晶界上的顯微結構變化依序為： $(\text{M}_7\text{C}_3 \text{ 碳化物} + \text{D0}_3) \rightarrow (\text{M}_7\text{C}_3 \text{ 碳化物} + \text{B2}) \rightarrow (\text{M}_7\text{C}_3 \text{ 碳化物} + \alpha)$ 。此現象至今從未被其他學者在 FeMnAlC 以及 FeMnAlCrC 合金系統中發現過。
- (二)、在淬火狀態下，Fe-30wt.%Mn-7wt.%Al-xwt.%Cr-1wt.%C alloys ( $x=0, 3, 6$  和 9) 合金的顯微結構為單一沃斯田鐵相。經過電化學腐蝕測試的研究發現，除了不含鉻的合金之外，其餘合金都能發現有明顯的鈍化

區。在鉻的添加不超過 6 wt.% 時，腐蝕電位及孔蝕電位皆會隨著鉻含量的增加而明顯的上昇。但是當鉻含量增加到 9 wt.% 時，腐蝕電位及孔蝕電位皆會下降。造成此抗腐蝕性質變差的原因是由於在沃斯田鐵基地內和晶界上有  $(\text{Fe},\text{Mn},\text{Cr})_7\text{C}_3$  碳化物析出。對於高鉻含量 ( $\text{Cr} \geq 3\text{wt.}\%$ ) FeMnAlCrC 的抗腐蝕性質研究從未在以前的文獻中被發表過。

(三)、在淬火狀態下，Fe-30wt.%Mn-10wt.%Al-4st.%Cr-0.45wt.%C 合金的顯微結構為(肥粒鐵 + 沃斯田鐵)之混合相。當此合金在 550°C 做時效處理後，Hägg 碳化物 ( $\text{M}_5\text{C}_2$ -type 碳化物) 會在  $\text{D0}_3$  區域的  $a/2 \langle 100 \rangle$  反向晶界上析出。此種 Hägg 碳化物至今從未被其他學者在 FeMnAlC 以及 FeMnAlCrC 合金系統中發現過。利用穿透式電子顯微鏡以及擇區繞射技術，Hägg 碳化物與  $\text{D0}_3$  基地之間的方向關係為： $(\bar{5}10)_{\text{M}_5\text{C}_2} // (1\bar{1}0)_{\text{D0}_3}$  以及  $(13\bar{4})_{\text{M}_5\text{C}_2} // (10\bar{2})_{\text{D0}_3}$ 。Hägg 碳化物和  $\alpha$ -type ( $\alpha, \text{D0}_3, \text{B2}$ ) 相間的方向關係也從未被其他學者中發現過。

(四)、Fe-30wt.%Mn-10wt.%Al-4st.%Cr-0.45wt.%C 合金在固溶處理並急速淬火後，其顯微結構為(肥粒鐵 + 沃斯田鐵)之混合相。當此合金經過 650°C 時效處理後，細微的  $(\text{Fe},\text{Mn})_3\text{AlC}$  碳化物 ( $k'$  碳化物) 會在沃斯田鐵相基地內形成。此外，隨著時效時間的延長，在肥粒鐵基地內的顯微結構之變化依序為： $(\text{B2} + \text{Hägg 碳化物}) \rightarrow (\text{B2} + \text{Hägg 碳化物} + \beta\text{-Mn}) \rightarrow (\text{B2} + \text{Hägg 碳化物} + \beta\text{-Mn} + \text{M}_{23}\text{C}_6 \text{ 碳化物})$ 。此種顯微結

構之變化至今從未被其他學者在 FeMnAlC 以及 FeMnAlCrC 合金系統中發現過。



# Phase Transformations and Corrosion Behaviors in Fe-Mn-Al-Cr-C Alloys

Student: Yi-Hsuan Tuan

Advisors: Prof. Tzeng-Feng Liu

Prof. Chuen-Guang Chao

Department of Materials Science and Engineering

National Chao Tung University

## Abstract

Phase transformations and corrosion behaviors in the fully austenitic and ( $\alpha$  +  $\gamma$ ) duplex FeMnAlCrC alloys have been investigated by means of scanning electron microscopy, transmission electron microscopy and energy-dispersive X-ray spectrometry. On the basis of the experimental examinations, the results can be summarized as follows:

- [1] The as-quenched microstructure of the Fe-30wt.%Mn-9wt.%Al-5wt.%Cr-0.7wt.%C alloy was single-phase austenite. When the as-quenched alloy was aged at 550°C-750°C, fine (Fe,Mn)<sub>3</sub>AlC carbides ( $k'$  carbides) were formed within the austenite matrix. In addition, as the aging temperature increased, a  $M_7C_3$  carbide +  $D0_3 \rightarrow M_7C_3$  carbide + B2  $\rightarrow M_7C_3$  carbide +  $\alpha$  (ferrite) phase transition had occurred on the grain boundaries. This grain boundary precipitation behavior has never been observed in FeMnAlC and

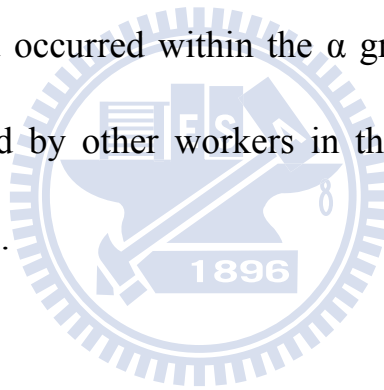
FeMnAlCrC alloy systems before.

- [2] The as-quenched microstructure of the Fe-30wt.%Mn-7wt.%Al-xwt.%Cr-1wt.%C alloys (x=0, 3, 6 and 9) was single-phase austenite. The electrochemical corrosion properties of the present alloys in 3.5% NaCl solution have been investigated. An obvious passivation could be observed for all the alloys except for the alloy without Cr content. The corrosion potential ( $E_{\text{corr}}$ ) and pitting potential ( $E_{\text{pp}}$ ) increased pronouncedly with increasing Cr content up to 6wt.%, and decreased as Cr content up to 9wt.%. The decrease of  $E_{\text{corr}}$  and  $E_{\text{pp}}$  of the alloy containing 9wt% Cr was due to the formation of  $(\text{Fe,Mn,Cr})_7\text{C}_3$  carbides in the austenite matrix and on the grain boundaries. It is noted that the corrosion behaviors of the austenitic Fe-Mn-Al-Cr-C alloys with higher Cr ( $\geq 3\text{wt.}\%$ ) content have never been reported in previous literatures.
- [3] The as-quenched microstructure of the Fe-30wt.%Mn-10wt.%Al-4st.%Cr-0.45wt.%C alloy was ( $\alpha + \gamma$ ) dual phases. When the alloy was aged at 550°C, Hägg carbides ( $\text{M}_5\text{C}_2$ -type carbides) occurred at  $a/2 \langle 100 \rangle$  anti-phase boundaries of the  $\text{D0}_3$  domains. The Hägg carbide has never been observed by previous workers in FeMnAlC and FeMnAlCrC alloy systems. By means of transmission electron microscopy and diffraction technique, the orientation relationship between Hägg carbide and  $\text{D0}_3$  matrix was



determined to be  $(\bar{5}10)_{M_5C_2} // (1\bar{1}0)_{D0_3}$  and  $(13\bar{4})_{M_5C_2} // (10\bar{2})_{D0_3}$ . The orientation relationship between Hägg carbide and bcc-type phase has also never been reported in previous literatures before.

- [4] The as-quenched microstructure of the Fe-30wt.%Mn-10wt.%Al-4wt.%Cr-0.45wt.%C alloy was  $(\alpha + \gamma)$  dual phases. When the as-quenched alloy was aged at 650°C, fine  $\kappa'$  carbides were formed within the  $\gamma$  grains. Additionally, with increasing the aging time at 650°C, a  $(B2 + \text{Hägg carbide}) \rightarrow (B2 + \text{Hägg carbide} + \beta\text{-Mn}) \rightarrow (B2 + \text{Hägg carbide} + \beta\text{-Mn} + M_{23}C_6 \text{ carbide})$  phase transition had occurred within the  $\alpha$  grain. This phase transition has never been observed by other workers in the FeMnAlC and FeMnAlCrC alloy systems before.



# Contents

	<u>page</u>
中文摘要 .....	i
Abstract .....	iv
Contents .....	vii
List of Tables .....	ix
List of Figures .....	x
<b>Chapter 1. General Introduction .....</b>	<b>1</b>
<b>Chapter 2. Grain boundary precipitation in Fe-30Mn-9Al-5Cr-0.7C alloy ..</b>	<b>11</b>
2-1 Introduction .....	13
2-2 Experimental procedure .....	15
2-3 Results and discussion .....	16
2-4 Conclusions .....	32
References .....	33
<b>Chapter 3. Corrosion behaviors of austenitic Fe-30Mn-7Al-xCr-1C alloys</b> <b>    in 3.5% NaCl solution .....</b>	<b>34</b>
3-1 Introduction .....	36
3-2 Experimental procedure .....	38
3-3 Results and discussion .....	41
3-4 Conclusions .....	53

References .....	54
<b>Chapter 4. Formation of Hägg carbide in an Fe-30Mn-10Al-4Cr-0.45C alloy ..</b>	<b>56</b>
<b>4-1</b> Introduction .....	58
<b>4-2</b> Experimental procedure .....	61
<b>4-3</b> Results and discussion .....	62
<b>4-4</b> Conclusions .....	76
References .....	77
<b>Chapter 5. Phase transformations in an Fe-30Mn-10Al-4Cr-0.45C alloy ..</b>	<b>79</b>
<b>5-1</b> Introduction .....	81
<b>5-2</b> Experimental procedure .....	84
<b>5-3</b> Results and discussion .....	85
<b>5-4</b> Conclusions .....	104
References .....	105
<b>List of Publications .....</b>	<b>107</b>

## **List of Tables**

Table 2.1 Chemical compositions of the phases identified by energy-dispersive X-ray spectrometer (EDS). .....	31
Table 3.1 Chemical compositions of the present alloys (wt.%) .....	40
Table 3.2 The electrochemical parameters from potentiodynamic polarization curves for the Fe-30wt.%Mn-7wt.%Al-(0, 3, 6 and 9)wt.%Cr-1wt.%C alloys in 3.5% NaCl solution. ....	47
Table 4.1 The d-spacings of the Hägg carbide. ....	70
Table 4.2 Angles among some reciprocal vectors of the Hägg carbide. ....	71
Table 4.3 Chemical compositions of the phases revealed by EDS. ....	72
Table 5.1 Chemical compositions of the phases revealed by energy-dispersive X-ray spectrometer (EDS). ....	102

## List of Figures

- Figure 2.1 Transmission electron micrographs of the alloy aged at 550°C for 6h.  
(a) BF, and (b) an SADP taken from a mixed region covering the austenite matrix and fine  $\kappa$  carbides. The zone axis is [001] ( $hkl$ : austenite matrix;  $\underline{hkl}$ :  $\kappa$  carbide) ..... 17
- Figure 2.2 Transmission electron micrographs of the alloy aged at 550°C for 24h.  
(a) BF, (b) an SADP taken from the  $D0_3$  phase marked “D” in (a). The zone axis is  $[01\bar{1}]$ , and (c) an SADP taken from the  $M_7C_3$  carbide marked “M” in (a). The zone axis is  $[11\bar{2}0]$ . ..... 18
- Figure 2.3 Transmission electron micrographs of the alloy aged at 550°C for 48h.  
(a) BF, (b)  $(100)_\kappa$  DF, (c) and (d) (111) and (200)  $D0_3$  DF, respectively. .... 22
- Figure 2.4 Transmission electron micrographs of the alloy aged at 650°C for 12h.  
(a) and (b) BF taken from the grain boundary and austenite matrix, respectively, (c) and (d) (111) and (200)  $D0_3$  DF, respectively. .... 24
- Figure 2.5 Transmission electron micrographs of the alloy aged at 750°C for 6h.  
(a) BF, (b) and (c) (111) and (200)  $D0_3$  DF, respectively. .... 26
- Figure 2.6 EDS spectra taken from (a)  $M_7C_3$  carbide, and (b)  $D0_3$  phase in the

alloy aged at 550°C for 48h. ....	30
Figure 3.1 Optical micrographs of the Fe-30wt.%Mn-7wt.%Al-(6, 9)wt.%Cr-1wt.%C alloys. (a) 6 wt.%Cr, and (b) 9 wt.%Cr. ....	43
Figure 3.2 Potentiodynamic polarization curves for the five Fe-30wt.%Mn-7wt.%Al-(0, 3, 6, and 9)wt.%Cr-1wt.%C alloys in 3.5% NaCl solution. ....	44
Figure 3.3 AES depth profiles for the passive film of the Fe-30wt.%Mn-7wt.%Al-(0, 6, and 9)wt.%Cr-1wt.%C alloys. (a) 0 wt.%Cr, (b) 6 wt.%Cr, and (c) 9 wt.%Cr. ....	45
Figure 3.4 Transmission electron micrographs of the Fe-30wt.%Mn-7wt.%Al-9wt.%Cr-1wt.%C alloy. (a) BF, and (b) a selected-area diffraction pattern taken from a $(\text{Fe,Mn,Cr})_7\text{C}_3$ carbide in (a). The zone axis of the $(\text{Fe,Mn,Cr})_7\text{C}_3$ carbide is $[\bar{1}2\bar{1}0]$ . (c) and (d) two typical EDS profiles obtained from the $(\text{Fe,Mn,Cr})_7\text{C}_3$ carbide and the $\gamma$ matrix nearby the $(\text{Fe,Mn,Cr})_7\text{C}_3$ carbide, respectively. ....	49
Figure 4.1 BF transmission electron micrograph taken from the $\gamma$ matrix of the alloy aged at 550°C for 12 h. ....	63
Figure 4.2 Transmission electron micrographs taken from the $\text{D0}_3$ matrix of the alloy aged at 550°C for 12 h. (a) BF, (b) an SADP, the zone axis is $[01\bar{1}]$ , (c) and (d) (111) and (200) $\text{D0}_3$ DF image, respectively, (e)	

(001) <sub>M<sub>5</sub>C<sub>2</sub></sub> DF image. ....	64
Figure 4.3 Eight SADPs taken from the precipitate marked “C” in Figure 4.2(a). The zone axes are (a) [110], (b) [210], (c) [1 $\bar{1}$ 0], (d) [3 $\bar{1}$ $\bar{2}$ ], (e) [10 $\bar{1}$ ], (f) [31 $\bar{4}$ ], (g) [11 $\bar{2}$ ] and (h) [22 $\bar{3}$ ], respectively. ....	69
Figure 4.4 Two SADPs taken from an area including the precipitate marked “C” in Figure 4.2(a) and its surrounding matrix. The zone axes are (a) [152] <sub>M<sub>5</sub>C<sub>2</sub></sub> , [110] <sub>D<sub>03</sub></sub> and (b) [154] <sub>M<sub>5</sub>C<sub>2</sub></sub> , [221] <sub>D<sub>03</sub></sub> , respectively. (hkl=M <sub>5</sub> C <sub>2</sub> carbide; $\underline{hkl}$ =D <sub>03</sub> phase) .....	75
Figure 5.1 Transmission electron micrographs of the as-quenched alloy. (a) an SADP taken from the $\alpha$ grain. The zone axis is [01 $\bar{1}$ ] ( $\underline{hkl}$ : $\alpha$ phase, hkl: D <sub>03</sub> phase). (b) and (c) (111) and (200) D <sub>03</sub> DF image, respectively. ....	87
Figure 5.2 Transmission electron micrographs of the alloy aged at 650°C for 6 h. (a) BF taken from the $\gamma$ grain. (b) BF taken from the $\alpha$ grain. (c) and (d) (111) and (200) D <sub>03</sub> DF images, respectively. ....	89
Figure 5.3 (a) through (c) Three SAPDs taken from the precipitate marked “C” in Figure 5.2(b). The zone axes are (a) [1 $\bar{1}$ 0], (b) [10 $\bar{1}$ ] and (c) [11 $\bar{2}$ ], respectively. ....	91

Figure 5.4 (a) SEM image of the alloy aged at 650°C for 12 h. (b) SADP taken from the precipitate marked “B” in Figure 5.4(a). The zone axis is [001]. (c) through (d) Three SADPs taken from an area including the precipitate marked “B” in Figure 5.4(a) and its surrounding matrix. The zone axes are (c)  $[001]_{\beta\text{-Mn}}$ ,  $[0\bar{1}2]_{\text{B}_2}$ , (d)  $[012]_{\beta\text{-Mn}}$ ,  $[001]_{\text{B}_2}$  and (e)  $[031]_{\beta\text{-Mn}}$ ,  $[011]_{\text{B}_2}$ , respectively. .... 93

Figure 5.5 (a) SEM image of the alloy aged at 650°C for 18 h. (b) through (e) Transmission electron micrographs of the alloy aged at 650°C for 18 h. (b) BF. (c) through (e) Three SADPs taken from the precipitate marked “P” in Figure 5.5(b). The zone axes are (c) [010], (d) [011] and (e) [111], respectively. .... 96

Figure 5.6 SEM image of the alloy aged at 650°C for 36 h. .... 101



# Chapter 1.

## General Introduction



## **General Introduction**

Phase transformations, mechanical properties and corrosion resistance in fully austenitic FeMnAlC alloys have been extensively studied by many workers [1-34]. In these studies, it is seen that the as-quenched microstructure of the FeMnAlC alloys with a chemical composition in the range of Fe-(26-34)wt.%Mn-(6-11)wt.%Al-(0.54-1.3)wt.%C was single-phase austenite ( $\gamma$ ). When the as-quenched alloys were aged at 500~750°C for moderate times, fine and coarse (Fe,Mn)<sub>3</sub>AlC carbide having an L'1<sub>2</sub>-type structure could be observed to precipitate coherently within the  $\gamma$  matrix and heterogeneously on the  $\gamma/\gamma$  grain boundaries, respectively. For convenience, the  $\kappa'$  carbide and  $\kappa$  carbide were used to represent the (Fe,Mn)<sub>3</sub>AlC carbide formed coherently within the  $\gamma$  matrix and heterogeneously on the  $\gamma/\gamma$  grain boundaries [8]. After prolonged aging time within this temperature range, the coarse  $\kappa$  carbide would grow into adjacent  $\gamma$  grains through a  $\gamma \rightarrow \alpha$  (ferrite) +  $\beta$ -Mn reaction, a  $\gamma \rightarrow \gamma_0$  (carbon-deficient austenite) +  $\kappa$  reaction, a  $\gamma \rightarrow \beta$ -Mn +  $\kappa$  reaction or a  $\gamma \rightarrow \alpha$  +  $\beta$ -Mn +  $\kappa$  reaction on the grain boundaries in the fully austenitic FeMnAlC alloys, depending on the chemical composition and aging temperature [5-10].

Additionally, in the previous studies [1-14], it was reported that the as-quenched microstructure of the Fe-(26-34)wt.%Mn-(7.8-10)wt.%Al-(0-1.75)wt.%M(M=Nb+V+Mo+W)-(0.85-1.3)wt.%C alloys was single  $\gamma$  phase or  $\gamma$

phase with small amount of (Nb,V)C carbides [1-14]. In the as-quenched condition, the alloys show various ultimate tensile strength (UTS) ranging from 840 to 950 MPa, yield strength (YS) ranging from 410 to 550 MPa and elongation from 70 to 57%, depending on the chemical composition [8, 11-25]. Based on these previous studies, it can be generally concluded that due to the formation of the fine  $k'$  carbides within the  $\gamma$  matrix and no precipitates on the grain boundaries, the alloys could possess an optimal combination of strength and ductility when the as-quenched alloys were aged at 550°C for about 16 h [8-10, 14]. With an elongation better than about 30%, the values of UTS and YS could be attained to be 953~1259 MPa and 665~1094 MPa, respectively [8-10, 14-15].

In addition to extensive studies of FeMnAlC alloys with  $C \leq 1.3$  wt.%, the phase transformations in the FeMnAlC alloys with higher carbon content have also examined by several workers [15, 35-38]. In their studies, it is obvious that the as-quenched microstructure of Fe-(26-30.7)wt.%Mn-(6-9)wt.%Al-(1.5-2.8)wt.%C alloys was  $\gamma$  phase containing fine  $\kappa'$  carbides [15, 35-38]. The fine  $\kappa'$  carbides were formed by spinodal decomposition during quenching [35-38]. This is quite different from that observed by other workers in the austenitic FeMnAlC alloys with  $C \leq 1.3$  wt.%. After being aged at 550~1150°C, the fine  $\kappa'$  carbides grew and a  $\gamma \rightarrow \gamma_0 + \kappa$  carbide reaction started to occur on the  $\gamma/\gamma$  grain

boundaries [15, 35-36]. The UTS, YS and elongation of the as-quenched FeMnAlC alloys with  $1.8 \leq C \leq 2.0$  wt.% were 1080~1105 MPa, 868~883 MPa and 55.5~54.5 %, respectively [37-38]. Obviously, with equivalent elongation, the mechanical strength was much higher than that examined in the as-quenched FeMnAlC alloys with  $C \leq 1.3$  wt.%. Furthermore, after being aged 450~550°C for moderate times, the alloys could possess high UTS ranging from 1395 to 1552 MPa and YS ranging from 1262 to 1423 MPa with a good elongation ranging from 32.5 to 25.8 % [37-38].

The as-quenched microstructure of the FeMnAlC alloys with  $0.4 \leq C \leq 0.51$  wt.% was  $(\alpha + \gamma)$  dual phases [11, 39-40]. When the alloys were aged at 550~710°C for moderate times, fine  $\kappa'$  carbide were found to precipitate within the  $\gamma$  matrix, and coarse  $\kappa$  carbides as well as  $\beta$ -Mn precipitates could be observed within the  $\alpha$  grains and on the  $\alpha/\alpha$  grain boundaries [39-40]. In 1991, the present workers examined the microstructural developments of an Fe-28.6wt.%Mn-10.1wt.%Al-0.46wt.%C alloy [41]. Consequently, it was found that in the as-quenched condition, extremely fine  $D0_3$  domains could be observed within the  $\alpha$  grains. The extremely fine  $D0_3$  domains were formed by a continuous ordering transition during quenching. This is different from that reported by other workers in the  $(\alpha + \gamma)$  duplex FeMnAlC alloys. When the alloy was aged at temperatures ranging from 450°C to 750°C, the phase

transformation sequence occurring within the  $\alpha$  grain was found to be  $\alpha + D0_3 \rightarrow \alpha + D0_3 + \kappa \rightarrow \alpha + B2 + \kappa \rightarrow \alpha$  [41]. The tensile properties of  $(\alpha + \gamma)$  duplex FeMnAlC alloys have also been investigated by many worker before [11, 42-43]. In their studies, the UTS, YS and elongation of the alloys in as-quenched condition were ranging between 570~786 MPa, 240~472 MPa and 70~35 %, respectively [11, 42-43].

Although the austenitic FeMnAl(M)C alloys could possess a remarkable combination of strength and ductility, the corrosion resistance of the alloys in aqueous environments was not adequate for applications in industry [44-48]. In order to improve the corrosion resistance, Cr has been added to the austenitic FeMnAlC alloys [47-50]. Consequently, it was found that the  $E_{\text{corr}}$  and  $E_{\text{pp}}$  of the as-quenched austenitic Fe-(29.2-31.3)wt.%Mn-(7.1-9.1)wt.%Al-(2.8-6)wt.%Cr-(0.88-1.07)wt.%C alloys in 3.5% NaCl solution were ranging from -820 to -556 mV and from -240 to -27 mV, respectively [47-50]. The results were much better than the  $E_{\text{corr}}$  (-920~-789 mV) and  $E_{\text{pp}}$  (-500~-280 mV) of the austenitic as-quenched FeMnAlC alloys [44-48]. However, the improvement of corrosion resistance due to the addition of Cr was not obvious in the  $(\alpha + \gamma)$  duplex FeMnAlCrC alloys [44, 51-52].

In contrast to the studies of the corrosion resistance, information concerning the microstructural developments of the austenitic and  $(\alpha + \gamma)$  duplex

FeMnAlCrC alloys is very deficient. Therefore, the purpose of the present study is an attempt to investigate the microstructural evolutions and corrosion behaviors of the austenitic and ( $\alpha + \gamma$ ) duplex FeMnAlCrC alloys by using OM, SEM, TEM, Auger electron spectroscopy (AES) and X-ray photoelectron spectroscopy (XPS), Potentiostat/Galvanostat and energy dispersive X-ray spectrometer (EDS) analyses. The detailed experiment results are presented in Chapters 2 through 5.



## References

1. K. Sato, K. Tagawa, Y. Inoue, *Scripta Metall.* 22 (1988) 899.
2. T.F. Liu, J.S. Chou, C.C. Wu, *Metal. Trans. A* 21 (1990) 1891.
3. K.H. Han, J.C. Yoon, W.K. Choo, *Scripta Metall.* 20 (1986) 33.
4. C.N. Hwang, T.F. Liu, *Scripta Mater.* 36 No.8 (1997) 853.
5. C.Y. Chao, C.N. Hwang, T.F. Liu, *Scripta Metall.* 28 (1993) 109.
6. K. Sato, K. Tagawa, Y. Inoue, *Metal. Trans. A* 21 (1990) 5.
7. C.N. Hwang, C.Y. Chao, T.F. Liu, *Scripta Metall.* 28 (1993) 263.
8. W.K. Choo, J.H. Kim, J.C. Yoon, *Acta Mater.* 45 (1997) 4877.
9. I.S. Kalashnikov, O. Acselrad, A. Shalkevich, *J. Mater. Process. Technol.* 136 (2003) 72.
10. G.S. Krivonogov, M.F. Alekseyenko and G.G. Solovyeva, *Fiz. Metal. Metalloved* 39 No.4 (1975) 775.
11. S.C. Tjong, S.M. Zhu, *Mater. Trans.* 38 No.2 (1997) 112.
12. I.S. Kalashnikov, O. Aksel'rad, M.S. Khadyev, *Metal Sci. Heat Treat.* 48 (2006) 5.
13. Kalashnikov, O. Acselrad, A. Shalkevich, L.C. Pereira, *J. Mater. Eng. Perform.* 9 (2000) 597.
14. I.S. Kalashnikov, B.S. Ermakov, O. Aksel'rad, L.K. Pereira, *Metal Sci. Heat Treat.* 43 No.11-12 (2001) 493.

15. Y. Kimura, K. Handa, K. Hayashi, Y. Mishima, *Intermetallics* 12 (2004) 607.
16. S.K. Banerji, *Met. Prog.* (1987) 59.
17. H.W. Leavenworth, Jr. and J.C. Benz, *J. Met.* (1985) 36.
18. J. Charles, A. Berghezan, A. Lutts, P.L. Dancoisne, *Met. Prog.* (1981) 71.
19. R. Wang, F.H. Beck, *Met. Prog.* (1983) 72.
20. J.C. Garcia, N. Rosas, R.J. Rioja, *Met. Prog.* (1982) 47.
21. D.J. Schmatz, *Trans. ASM.* 52 (1960) 898.
22. M.F. Alekseyenko, G.S. Krivonogov, L.G. Kozyreva, I.M. Kachanova, L.V. Arapova, *Met. Sci. Heat Treat.* 14 No.3-4 (1972) 187.
23. L.I. Lysak, M.F. Alekseyenko, A.G. Drachinskaya, N.A. Storchak, G.S. Krivonogov, *Metallofizika* 59 No.4 (1975) 29.
24. R.E. Cairns, Jr. and J.L. Ham, U.S. patent, No. 3111405 (1963).
25. I. Briggs, G.J. Russell, A.G. Clegg, *J. Mater. Sci.* 20 (1985) 668.
26. W.K. Choo, K.H. Han, *Metall. Trans. A* 16 (1985) 5.
27. W.K. Choo, D.G. Kim, *Metall. Trans. A* 18 (1987) 759.
28. S.C. Tjong, N.G. Ho, *Metallography* 21 (1988) 199.
29. G.L. Kayak, *Met. Sci. Heat Treat.* 22 No.2 (1969)95.
30. S.M. Zhu, S.C. Tjong, *Metall. Trans. A* 29 (1998)299.
31. I.S. Kalashnikov, O. Acselrad, L.C. Pereira, T. Kalichak, M.S. Khadyev, J.



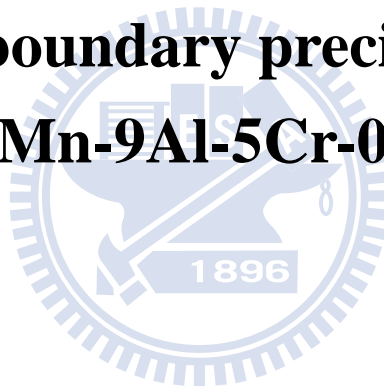
- Mater. Eng. Perform. 9 (2000)334.
32. S.C. Tjong, C.S. Wu, Mater. Sci. Eng. 80 (1986) 203.
  33. I.F. Tsu, T.P. Perng, Metall. Trans. A 22 (1991) 215.
  34. S.M. Zhu, S.C. Tjong, Scripta 36 (1997) 317.
  35. K. Ishida, H. Othani, N. Statoh, R. Kainuma, T. Nishizawa, ISIJ International 30 (1990) 680.
  36. C.S. Wang, C.N. Hwang, C.G. Chao, T.F. Liu, Scripta Mater. 57 (2007) 809.
  37. K.M. Chang, C.G. Chao, T.F. Liu, Scripta Mater. 63 (2010) 162.
  38. C.L. Lin, C.G. Chao, H.Y. Bor, T.F. Liu, Mater. Trans. 51 No.6 (2010) 1084.
  39. S.C. Tjong, N.J. Ho, Metallography 21 (1988) 1996.
  40. T.F. Liu, C.M. Wan, Strength Met. Alloys 1 (1986) 423.
  41. C.C. Wu, J.S. Chou, T.F. Liu, Metall. Trans. A 22A (1991) 2265.
  42. K.S. Chan, L.H. Chen, T.S. Lui, Mater. Trans. 38 No.5 (1997) 420.
  43. S.C. Chang, Y.H. Hsiau, M.T. Jahn, J. Mater. Sci. 24 (1989) 1117.
  44. M. Ruscak, T.P. Perng, Corrosion Oct. (1995) 738.
  45. W.T. Tsai, J.B. Duh, J.T. Lee, J. Mater. Sci. 22 (1987) 3517.
  46. J.B. Duh, W.T. Tsai, J.T. Lee, Corrosion Nov. (1988) 810.
  47. S.C. Chang, J.Y. Liu, H.K. Juang, Corrosion 51 No.5 (1995) 399.
  48. C.J. Wang, Y.C. Chang, Mater. Chem. Phys. 76 (2002) 151.
  49. C.S. Wang, C.Y. Tsai, C.G. Chao, T.F. Liu, Mater. Trans. 48 (2007) 2973.

50. Y.H. Tuan, C.S. Wang, C.Y. Tsai, C.G. Chao, T.F. Liu, Mater. Chem. Phys. 114 (2009) 595.
51. S.C. Chang, W.H. Weng, H.C. Chen, S.J. Lin, P.C.K. Chung, Wear 181-183 (1995) 511.
52. S.T. Shih, C.Y. Tai, T.P. Perng, Corrosion Feb (1993) 130.



# **Chapter 2.**

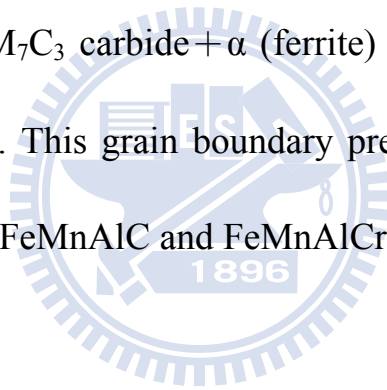
## **Grain boundary precipitation in Fe-30Mn-9Al-5Cr-0.7C alloy**



# Grain boundary precipitation in Fe-30Mn-9Al-5Cr-0.7C alloy

## Abstract

The as-quenched microstructure of the Fe-30wt.%Mn-9wt.%Al-5wt.%Cr-0.7wt.%C alloy was single-phase austenite. When the as-quenched alloy was aged at 550~750°C, fine (Fe,Mn)<sub>3</sub>AlC carbides were formed within the austenite matrix. In addition, as the aging temperature increased, a M<sub>7</sub>C<sub>3</sub> carbide + D0<sub>3</sub> → M<sub>7</sub>C<sub>3</sub> carbide + B2 → M<sub>7</sub>C<sub>3</sub> carbide + α (ferrite) phase transition had occurred on the grain boundaries. This grain boundary precipitation behavior has never before been observed in FeMnAlC and FeMnAlCrC alloy systems.



## **2-1 Introduction**

Phase transformations in austenitic FeMnAlC alloys have been extensively studied by many workers [1-8]. These studies have shown that in the as-quenched condition, the microstructure of the alloy with a chemical composition in the range of Fe-(26-34)wt.%Mn-(6-11)wt.%Al-(0.54-1.3)wt.%C was single-phase austenite ( $\gamma$ ). After being aged at 500-750°C for moderate times, fine and coarse (Fe,Mn)<sub>3</sub>AlC carbides ( $\kappa$  carbides) having an L'1<sub>2</sub>-type structure were observed to precipitate coherently within the austenite matrix and also heterogeneously on the austenite grain boundaries, respectively. With increasing aging time within this temperature range, the coarse  $\kappa$  carbides grew into the adjacent austenite grains through a  $\gamma \rightarrow \gamma_0$  (carbon-deficient austenite) +  $\kappa$  carbide reaction, a  $\gamma \rightarrow \alpha + \kappa$  carbide reaction, a  $\gamma \rightarrow \kappa$  carbide +  $\beta$ -Mn reaction, or a  $\gamma \rightarrow \alpha + \kappa$  carbide +  $\beta$ -Mn reaction [5-8], depending on the chemical composition and aging temperature. In order to improve the corrosion resistance, chromium has been added to the austenitic FeMnAlC alloys [9-12]. In their studies, it was concluded that the chromium addition could effectively improve the corrosion resistance of the alloys. However, to date, information about the influence of Cr addition on the microstructural developments of the austenitic FeMnAlC alloys is very deficient. Therefore, the purpose of this work is an attempt to study the phase transformations in the Fe-30wt.%Mn-9wt.%Al-

5wt.%Cr-0.7wt.%C alloy.



## **2-2 Experimental procedure**

Fe-30wt.%Mn-9wt.%Al-5wt.%Cr-0.7wt.%C alloy, was prepared in an induction furnace by using commercial 99.9% Fe, Mn, Al, Cr and pure carbon powder under a controlled protective argon atmosphere. After being homogenized at 1250°C for 12h, the ingot was hot-forged and then cold-rolled to a final thickness of 3.0 mm. The sheet was subsequently solution heat-treated (S.H.T.) at 1050°C for 2h and then rapidly quenched into room temperature water. Isothermal aging was performed at 550-850°C for various times in a vacuum furnace and then quenched. Specimens for electron microscopy were prepared by means of a double-jet electropolisher with an electrolyte of 65% ethanol, 20% acetic acid and 15% perchloric acid. Electron microscopy was performed with JEOL 2000FX scanning transmission electron microscope (STEM) operating at 200 kV. This microscope was equipped with a Link ISIS 300 energy-dispersive X-ray spectrometer (EDS) for chemical analysis. Quantitative analyses of elemental concentrations for Fe, Mn, Al and Cr were made using the Cliff-Lorimer ratio thin section method.

## **2-3 Results and discussion**

Transmission electron microscopy examinations indicated that in the as-quenched condition, the microstructure of the alloy was single-phase austenite. Figure 2.1(a) is a bright-field (BF) electron micrograph of the alloy aged at 550°C for 6 h, revealing that fine precipitates with a modulated structure were formed along the  $\langle 100 \rangle$  directions within the austenite matrix and no evidence of precipitates could be detected on the grain boundary. A selected-area diffraction pattern (SADP) taken from a mixed region covering the austenite matrix and fine precipitates (Fig. 2.1(b)), demonstrates that the fine precipitates are  $(\text{Fe,Mn})_3\text{AlC}$  carbides ( $\kappa$  carbides) having an  $L'1_2$  structure [4-7]. After prolonged aging at 550°C, a heterogeneous reaction started to occur on the grain boundaries. A typical microstructure is illustrated in Fig. 2.2(a). Figures 2.2(b) and (c) are two SADPs taken from the precipitates marked as “D” and “M” in Fig. 2.2(a), indicating that the two kinds of coarse precipitates were of  $\text{D0}_3$  phase and  $(\text{Fe,Mn,Cr})_7\text{C}_3$  (designated as  $\text{M}_7\text{C}_3$ ) carbide, respectively [3, 13]. This result indicates that the precipitation of ( $\text{M}_7\text{C}_3$  carbide +  $\text{D0}_3$  phase) had occurred on the grain boundaries. By increasing the aging time at the same temperature, the precipitation would proceed toward the inside of the austenite grains, as illustrated in Fig. 2.3. Figure 2.3(a) is a BF electron micrograph of the



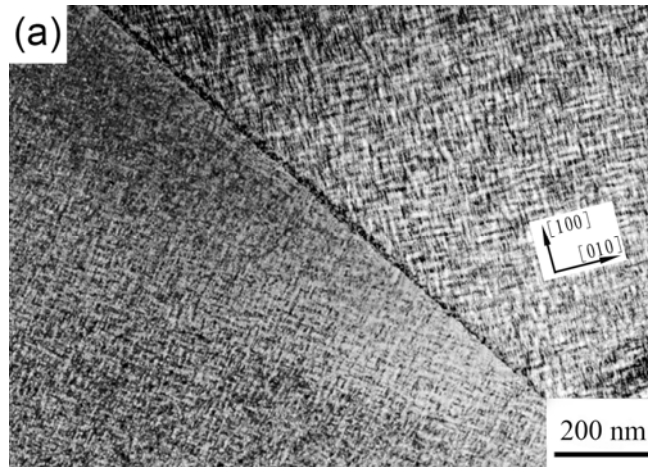


Figure 2.1 (a)

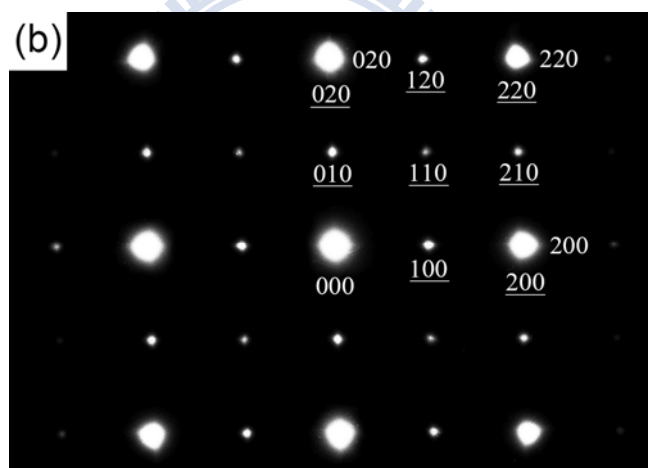


Figure 2.1 (b)

Figure 2.1 Transmission electron micrographs of the alloy aged at 550°C for 6h. (a) BF, and (b) an SADP taken from a mixed region covering the austenite matrix and fine  $\kappa$  carbides. The zone axis is [001] (hkl: austenite matrix; hkl:  $\kappa$  carbide)

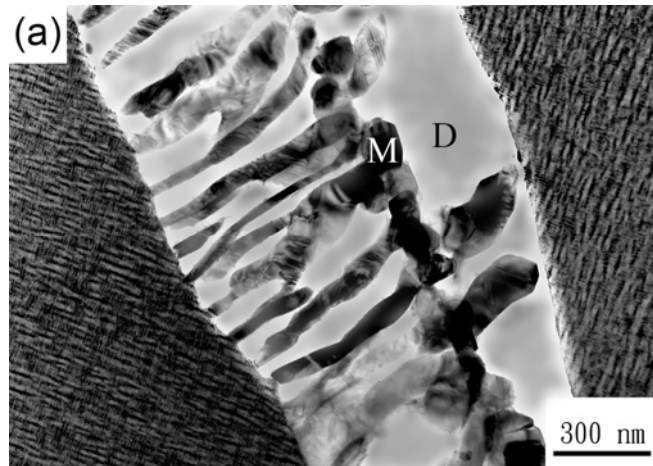


Figure 2.2 (a)

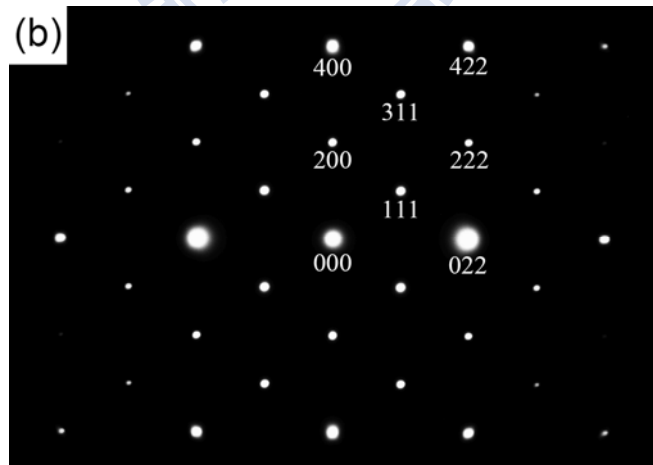


Figure 2.2 (b)

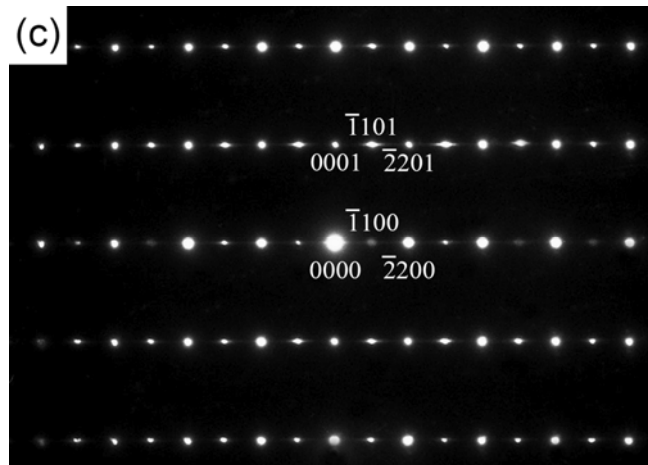


Figure 2.2 (c)

Figure 2.2 Transmission electron micrographs of the alloy aged at 550°C for 24h. (a) BF, (b) an SADP taken from the  $D0_3$  phase marked “D” in Figure 2.2(a). The zone axis is  $[01\bar{1}]$ , and (c) an SADP taken from the  $M_7C_3$  carbide marked “M” in (a). The zone axis is  $[11\bar{2}0]$ .

alloy aged at 550°C for 48h, revealing that the precipitation of ( $M_7C_3$  carbide +  $D0_3$  phase) has a lamellar structure. Figure 2.3(b) is a  $(100)_\kappa$  dark-field (DF) electron micrograph, revealing the presence of fine  $\kappa$  carbides within the austenite matrix. Figures 2.3(c) and (d) are  $(111)$  and  $(200)$   $D0_3$  enlarged DF electron micrographs, clearly revealing that the  $(111)$   $D0_3$  DF image and  $(200)$   $D0_3$  DF image are morphologically identical. Since the  $(200)$  reflection spot comes from both the B2 and  $D0_3$  phases, while the  $(111)$  reflection spot comes only from the  $D0_3$  phase [14], the bright precipitates presented in Figs. 2.3(c) and (d) are considered to be  $D0_3$  phase.

When the alloy was aged at 650°C, the morphology of the grain boundary  $M_7C_3$  carbides changed from plate-like to granular shape, as shown in Fig. 2.4(a). Figure 2.4(b) is a BF electron micrograph taken from the austenite matrix, showing that the amount of the fine  $\kappa$  carbides within the austenite matrix was drastically decreased. Figures 2.4(c) and (d) are  $(111)$  and  $(200)$   $D0_3$  enlarged DF electron micrographs of the grain boundary, revealing the presence of the extremely fine  $D0_3$  and large B2 domains, respectively. Since the size of the  $D0_3$  domains is extremely fine, it is plausible to suggest that the extremely fine  $D0_3$  domains were formed by a  $B2 \rightarrow D0_3$  ordering transition during quenching from the aging temperature [14]. It means that the grain boundary microstructure of the alloy present at 650°C was a mixture of ( $M_7C_3$  carbide + B2). Transmission

electron microscopy of thin foils indicated that the precipitation of ( $M_7C_3$  carbide + B2) was preserved up to  $700^\circ\text{C}$ . Figures 2.5(a) through (c) are BF, (111) and (200)  $D0_3$  DF electron micrographs of the alloy aged at  $750^\circ\text{C}$  for 6h and then quenched, revealing that besides the presence of the  $M_7C_3$  carbide (marked as “M” in Fig. 2.5(a)), only extremely fine  $D0_3$  domains and small B2 domains could be observed on the grain boundaries. This indicates that the grain boundary microstructure of the alloy present at  $750^\circ\text{C}$  should be a mixture of ( $M_7C_3$  carbide +  $\alpha$ ), and the extremely fine  $D0_3$  domains and small B2 domains were formed by a  $\alpha \rightarrow \text{B2} \rightarrow D0_3$  continuous ordering transition during quenching [14]. Progressively higher temperature aging and quenching experiments indicated that the grain boundary precipitation of ( $M_7C_3$  carbide +  $\alpha$ ) could be observed up to  $800^\circ\text{C}$ . However, when the aging temperature was increased to  $850^\circ\text{C}$ , only single-phase austenite could be observed and no evidence of the grain boundary precipitation could be detected.

The fact that the phase transition of  $M_7C_3$  carbide +  $D0_3 \rightarrow M_7C_3$  carbide + B2  $\rightarrow M_7C_3$  carbide +  $\alpha$  had occurred on the grain boundaries in the alloy aged at  $550\sim 750^\circ\text{C}$  is a remarkable feature in the present study. This grain boundary precipitation behavior has never before been observed in FeMnAlC and FeMnAlCrC alloy systems. In order to clarify this feature, an STEM-EDS study

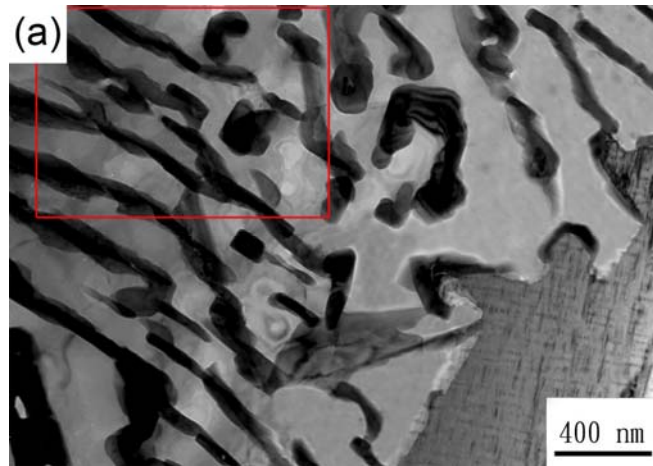


Figure 2.3 (a)

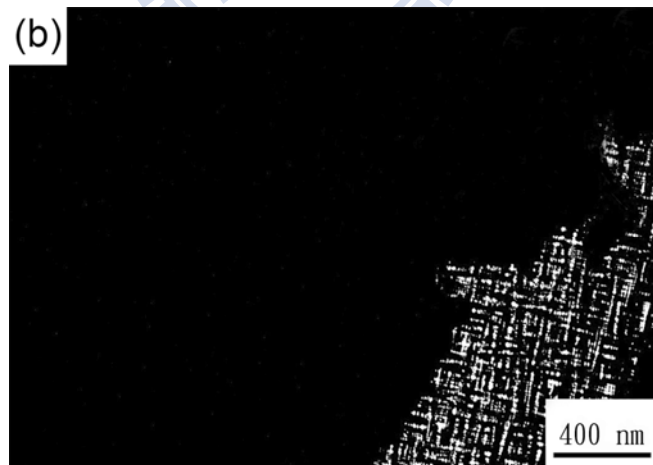


Figure 2.3 (b)

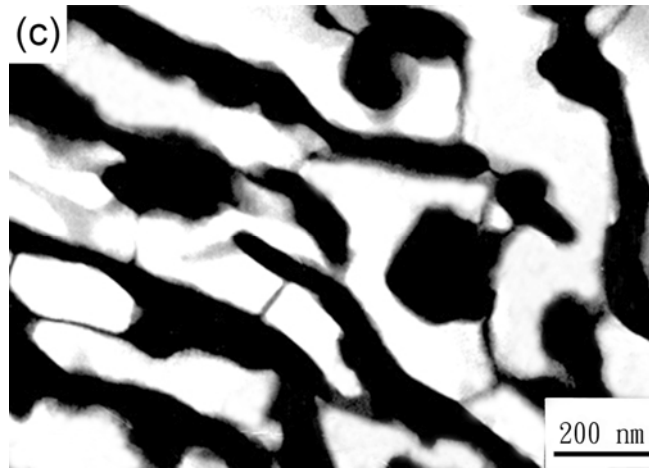


Figure 2.3 (c)

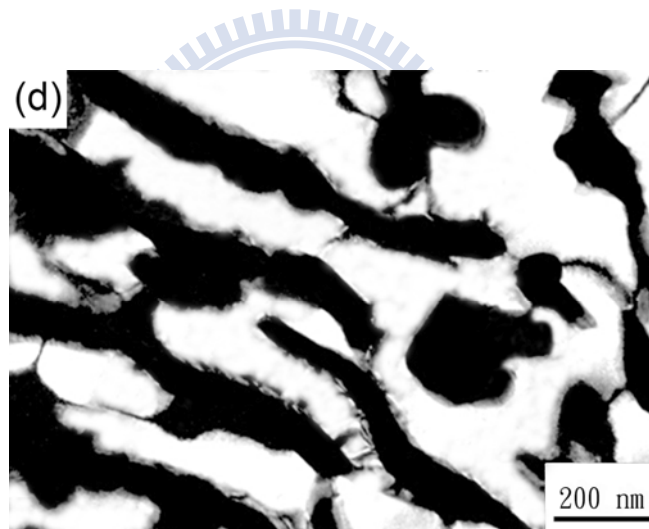


Figure 2.3 (d)

Figure 2.3 Transmission electron micrographs of the alloy aged at 550°C for 48h. (a) BF, (b)  $(100)_\kappa$  DF, (c) and (d)  $(111)$  and  $(200)$   $D0_3$  DF, respectively.

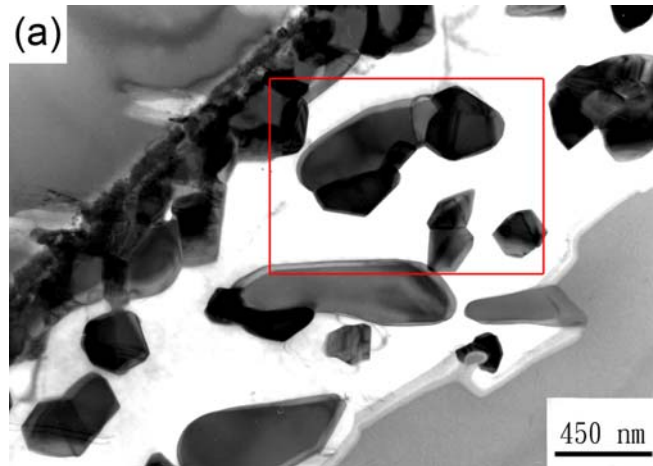


Figure 2.4 (a)

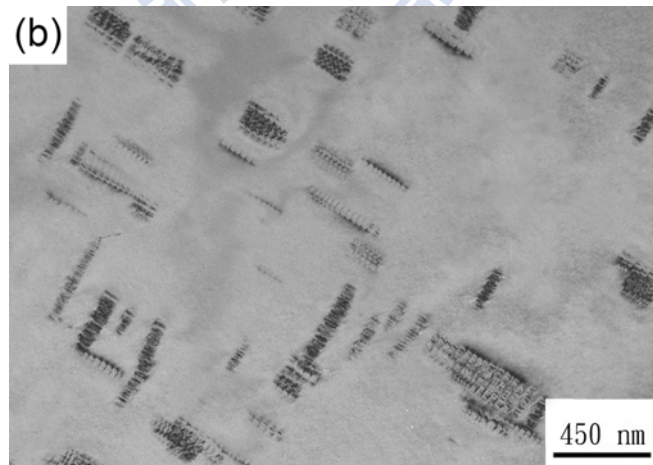


Figure 2.4 (b)



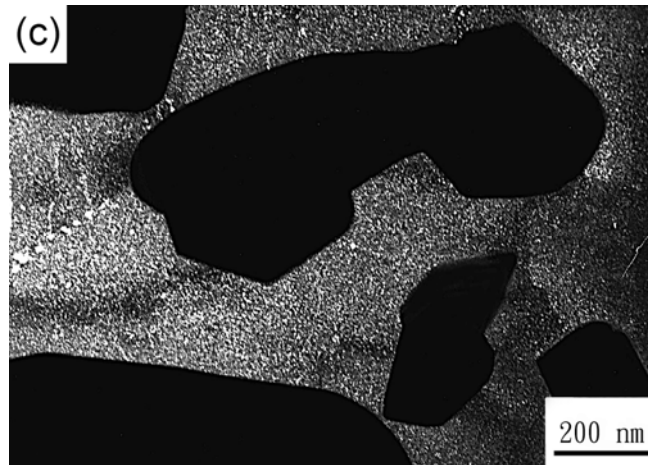


Figure 2.4 (c)

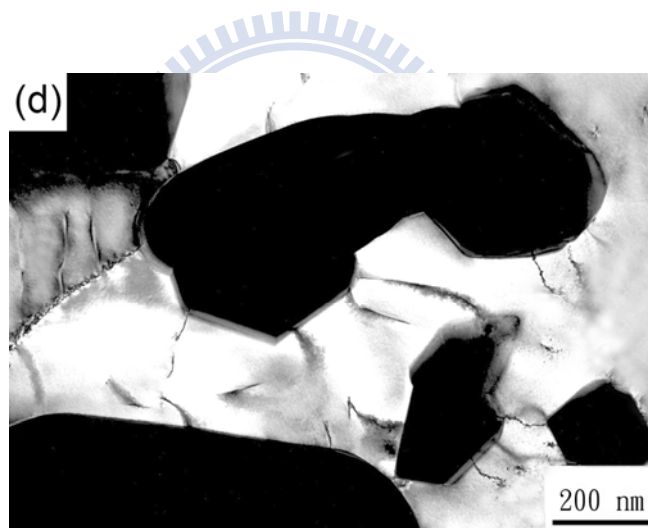


Figure 2.4 (d)

Figure 2.4 Transmission electron micrographs of the alloy aged at 650°C for 12h. (a) and (b) BF taken from the grain boundary and austenite matrix, respectively, (c) and (d) (111) and (200)  $D_0_3$  DF, respectively.

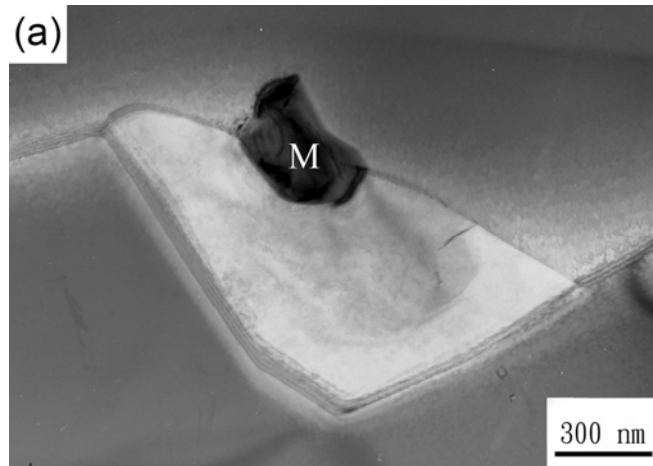


Figure 2.5 (a)

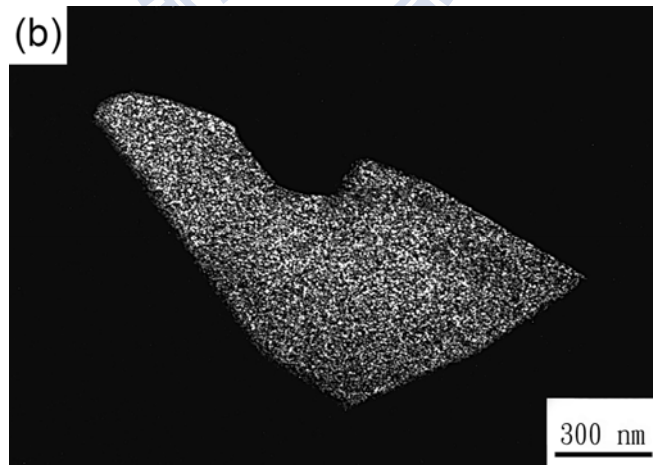


Figure 2.5 (b)

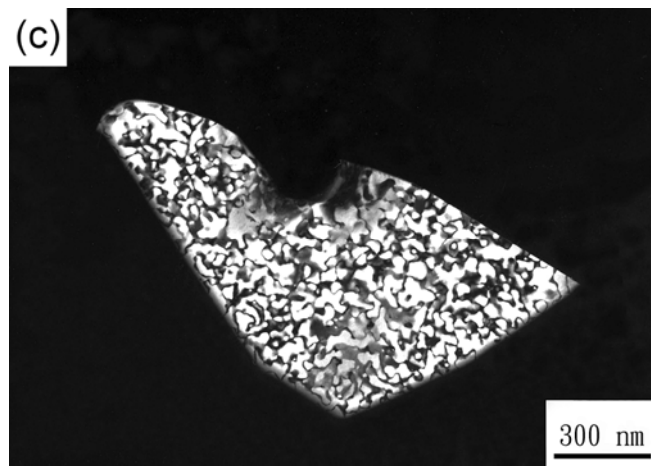


Figure 2.5 (c)

Figure 2.5 Transmission electron micrographs of the alloy aged at 750°C for 6h. (a) BF, (b) and (c) (111) and (200)  $D0_3$  DF, respectively.

was made. Figures 2.6(a) and (b) represent two typical EDS spectra taken from a  $M_7C_3$  carbide and the  $D0_3$  phase in the alloy aged at  $550^\circ\text{C}$  for 48h, where the Fe, Mn, Al, and Cr peaks were examined (EDS with a thick-window detector is limited to detect the elements of atomic number of 11 or above; therefore, carbon cannot be examined by this method). The quantitative chemical compositions of  $M_7C_3$  and  $D0_3$  phases from Figs. 2.6(a) and (b) are listed in Table 2.1. For the comparison, the chemical compositions of the  $M_7C_3$  carbide, B2 and  $\alpha$  phases in the alloy aged at different temperatures are also listed in Table 2.1. In Fig. 2.6 and Table 2.1, it is clearly seen that when the alloy was aged at  $550^\circ\text{C}$ , the Mn and Cr contents in the  $M_7C_3$  carbide are much higher than those of the as-quenched alloy, and the reverse result is obtained for the Al content. Since it is known that the Mn is an austenite former in the FeMnAlC alloy system, the precipitation of coarse Mn-rich  $M_7C_3$  carbide on the grain boundary would cause the austenite phase in the vicinity of the coarse  $M_7C_3$  carbides to become unstable. Furthermore, it is seen in Table 2.1 that the Al content in the  $M_7C_3$  carbide is only about 1.83 at.%, which is much less than that in the as-quenched alloy. It is thus anticipated that along with the precipitation of the  $M_7C_3$  carbides, the surrounding regions would be enriched in Al. In Fe-Al phase diagram [14], it is seen that when an Fe-26.31at.%Al alloy is heated at  $550^\circ\text{C}$ , the microstructure was a  $D0_3$  phase. Therefore, it is reasonable to believe

that owing to the enrichment of Al, the unstable austenite phase would be transformed into the  $D0_3$  instead of the  $\alpha$  phase. Similarly, when the alloy was aged at  $650^\circ\text{C}$  as well as  $750^\circ\text{C}$  and then quenched, the Al-rich B2 and  $\alpha$  phases could be formed at the regions contiguous to the  $M_7C_3$  carbides, and  $B2 \rightarrow D0_3$  as well as  $\alpha \rightarrow B2 \rightarrow D0_3$  ordering transitions would be expected to occur during quenching [14]. This is in agreement with the experimental observations in Figs. 2.4 and 2.5, respectively. Finally, it is worthwhile pointing out that the coarse Mn-rich  $\kappa$  carbides were always observed on the grain boundaries in the austenitic FeMnAlC alloys aged at  $500\sim 750^\circ\text{C}$  for longer times [5-8, 15]. However, only (Mn,Cr)-rich  $M_7C_3$  carbides were formed, and no evidence of coarse  $\kappa$  carbides could be detected on the grain boundaries in the present alloy aged at  $550\sim 750^\circ\text{C}$ . Obviously, the chromium addition in the austenitic FeMnAlC alloys would bring about for the formation of the (Mn,Cr)-rich  $M_7C_3$  carbides and suppress the precipitation of the coarse Mn-rich  $\kappa$  carbides on the grain boundaries.

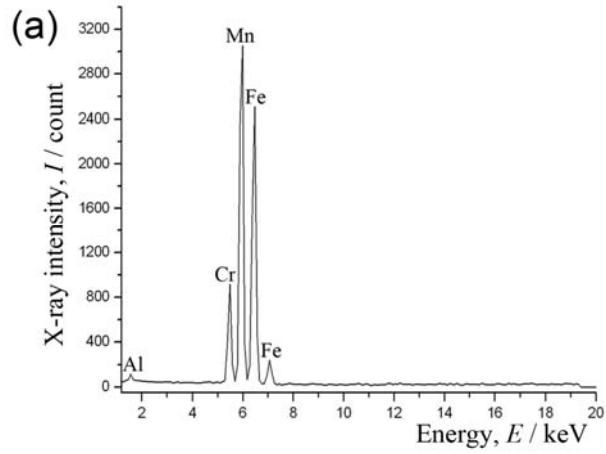


Figure 2.6 (a)

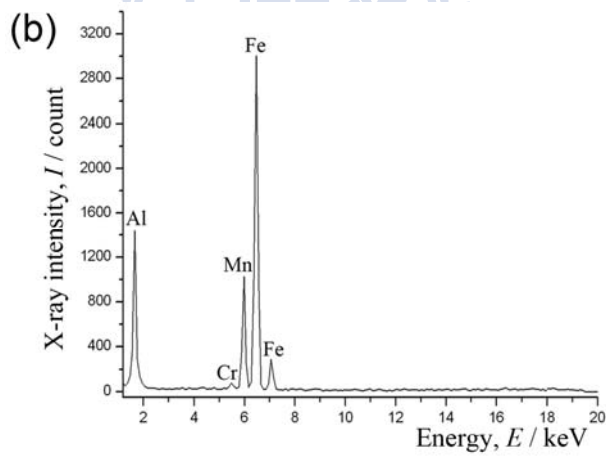


Figure 2.6 (b)

Figure 2.6 EDS spectra taken from (a)  $M_7C_3$  carbide, and (b)  $D0_3$  phase in the alloy aged at  $550^\circ\text{C}$  for 48h.

Table 2.1 Chemical compositions of the phases identified by energy-dispersive X-ray spectrometer (EDS).

Heat treatment	Phase	Chemical composition (at.%)			
		Fe	Mn	Al	Cr
S.H.T.	$\gamma$	50.68	27.60	16.86	4.86
550°C, 48h	D0 <sub>3</sub>	56.78	15.84	26.31	1.07
	M <sub>7</sub> C <sub>3</sub>	37.91	47.69	1.83	12.57
650°C, 12h	B2	55.62	16.17	26.95	1.26
	M <sub>7</sub> C <sub>3</sub>	37.87	46.76	1.75	13.62
750°C, 6hr	A2	53.57	17.12	27.13	2.18
	M <sub>7</sub> C <sub>3</sub>	37.09	46.15	1.63	15.13

## **2-4 Conclusions**

As-quenched microstructure of the Fe-30wt.%Mn-9wt.%Al-5wt.%Cr-0.7wt.%C alloy was single-phase austenite. When the as-quenched alloy was aged at 550~750°C, fine  $\kappa$  carbides were formed within the austenite matrix, and a  $M_7C_3 + D0_3 \rightarrow M_7C_3 + B2 \rightarrow M_7C_3 + \alpha$  phase transition had occurred on the grain boundaries.



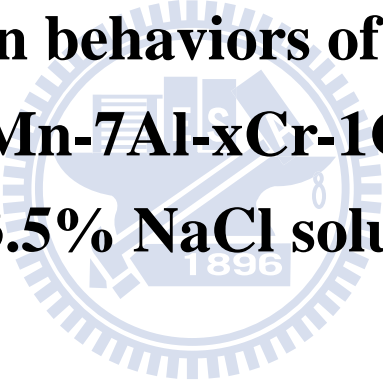


## References

1. S. Kalashnikov, O. Acselrad, A. Shalkevich, *J. Mater. Process. Technol.* 136 (2003) 72.
2. K. Sato, K. Tagawa, Y. Inoue, *Scripta Metall.* 22 (1988) 899.
3. T. F. Liu, J. S. Chou, C. C. Wu, *Metal. Trans. A* 21 (1990) 1891.
4. K. H. Han, J. C. Yoon, W. K. Choo, *Scripta Metall.* 20 (1986) 33.
5. C. Y. Chao, C. N. Hwang, T. F. Liu, *Scripta Metall.* 28 (1993) 109.
6. C. N. Hwang, C. Y. Chao, T. F. Liu, *Scripta Metall.* 28 (1993) 263.
7. W. K. Choo, J. H. Kim, J. C. Yoon, *Acta Mater.* 45 (1997) 4877.
8. K. Sato, K. Tagawa, Y. Inoue, *Metal. Trans. A* 21 (1990) 5.
9. C. S. Wang, C. Y. Tsai, C. G. Chao, T. F. Liu, *Mater. Trans.* 48 (2007) 2973.
10. S. C. Chang, J. Y. Liu, H. K. Juang, *Corros. Eng.* 51 (1995) 399.
11. S. C. Chang, W. H. Weng, H. C. Chen, S. J. Lin, P. C. K. Chung, *Wear* 181-183 (1995) 511.
12. C. J. Wang, Y. C. Chang, *Mat. Chem. Phys.* 76 (2002) 151.
13. F. Ernst, Y. Cao, G. M. Michal, *Acta Mater.* 52 (2004) 1469.
14. Samuel M. Allen, *Phil. Mag.* 36 (1977) 181.
15. C. S. Wang, C. N. Hwang, C. G. Chao, T. F. Liu, *Scripta Metall.* 57 (2007) 809.

# **Chapter 3.**

**Corrosion behaviors of austenitic  
Fe-30Mn-7Al-xCr-1C alloys  
in 3.5% NaCl solution**



# **Corrosion behaviors of austenitic Fe-30Mn-7Al-xCr-1C alloys in 3.5% NaCl solution**

## **Abstract**

The corrosion behaviors of the as-quenched Fe-30wt.%Mn-7wt.%Al-xwt.%Cr-1wt.%C alloys (x=0, 3, 6 and 9) in 3.5% NaCl have been investigated. Passivation could be observed for all the alloys except for the alloy without Cr content. The corrosion potential ( $E_{\text{corr}}$ ) and pitting potential ( $E_{\text{pp}}$ ) increased pronouncedly with increasing Cr content up to 6wt.%, and decreased as Cr content up to 9wt.%. The decrease of  $E_{\text{corr}}$  and  $E_{\text{pp}}$  of the alloy containing 9wt% Cr was due to the formation of  $(\text{Fe,Mn,Cr})_7\text{C}_3$  carbides in the austenite matrix and on the grain boundaries. It is noted that the corrosion behaviors of the austenitic Fe-Mn-Al-Cr-C alloys with higher Cr ( $\geq 3\text{wt.}\%$ ) content have never been reported in previous literatures.

### **3-1 Introduction**

The austenitic Fe-Mn-Al-C quaternary alloys have many advantages, such as low cost, low density, high strength, high toughness, and good oxidation resistance [1-6]. However, the corrosion resistance of the austenitic Fe-Mn-Al-C alloys in aqueous environments was not adequate for applications in industry [5-13]. Therefore, many researchers tried to improve the corrosion resistance of the austenitic Fe-Mn-Al-C alloys by adding chromium and decreasing carbon content [6,9,14-17]. Since Cr and C are ferrite and austenite formers in ferrous alloys, respectively, the Fe-Mn-Al-Cr-C alloys with higher Cr and lower C contents consist of (austenite + ferrite) dual phases. Some literatures showed that Fe-(21.5-27.7)wt.%Mn-(8.9-9.9)wt.%Al-(3.1-6.2)wt.%Cr-(0.33-0.42)wt.%C alloys exhibited austenite and ferrite dual phases, and the mechanical properties of the dual-phase Fe-Mn-Al-Cr-C alloys were far inferior to those of austenitic ones. In order to obtain full austenitic structure, a proper combination of chromium and carbon contents was treated. In the previous studies [5,6], it was reported that the Fe-(29.5-31.3)wt.%Mn-(8.4-8.9)wt.%Al-(2.6-2.8)wt.%Cr-(0.98-1.06)wt.%C alloys had a single-phase austenite, and the corrosion resistance of the austenitic Fe-Mn-Al-Cr-C alloys was indeed superior to that of the austenitic Fe-Mn-Al-C or dual-phase Fe-Mn-Al-Cr-C alloys. However, to date, information concerning the corrosion behaviors of the austenitic

Fe-Mn-Al-Cr-C alloys with higher Cr ( $\geq 3\text{wt.}\%$ ) content is very deficient. In this study, the electrochemical corrosion properties of four austenitic Fe-30wt.%Mn-7wt.%Al-1wt.%C alloys with 0, 3, 6 and 9 wt.% Cr contents in 3.5% NaCl solution were investigated to evaluate the effects of Cr content on the corrosion resistance.



## **3-2 Experimental procedure**

The chemical compositions of the alloys are shown in Table 3.1. The alloys were prepared by melting commercial pure Fe, Mn, Al, Cr and carbon powder in an induction furnace under a controlled protective argon atmosphere. The melt was cast into 30mm × 50mm × 200mm ceramic shell mold. After being homogenized at 1473K for 24 h, the ingots were sectioned into 12mm × 12mm × 5mm slices. These slices were subsequently solution heat-treated in vacuum furnace at 1373K for 2 h and then rapidly quenched into room-temperature water. Potentiodynamic polarization curves were measured in 3.5% NaCl solution at 298K. Electrochemical polarization curves were obtained by using an EG&G Princeton Applied Research Model 273 galvanostat/potentiostat. Specimens with an exposed surface area of ~1cm<sup>2</sup> were ground with 2000-grit SiC paper and then with 1.5μm Al<sub>2</sub>O<sub>3</sub> powder, washed in distilled water and rinsed in acetone prior to passivation. Potentiodynamic polarization curves were obtained at a potential scan rate of 5 mV/sec from -1 V to 0.5 V. The concentration of elements in the passive film was examined by Auger electron spectroscopy (AES) and X-ray photoelectron spectroscopy (XPS). As well known, the composition quantification of AES is very poor due to matrix effect, peaks overlapping and surface roughness, etc. However, the depth profiling is one of the most important and convenient application of AES

for analysing the composition of thin surface layer. Therefore, the depth profiling of AES is an appropriate and effective method for analysing the composition distributions of the passive film in this experiment [18,19]. Microstructures were examined by using optical microscopy and transmission electron microscopy (TEM). TEM specimens were prepared by means of a double-jet electropolisher with an electrolyte of 15% perchloric acid, 25% acetic acid and 60% ethanol. Electron microscopy was performed on JEOL-2000FX STEM operating at 200 kV. This microscope was equipped with a Link ISIS 300 energy-dispersive X-ray spectrometer (EDS) for chemical analysis. Quantitative analyses of elemental concentrations for Fe, Mn, Al and Cr were made using the Cliff-Lorimer ratio thin section method.

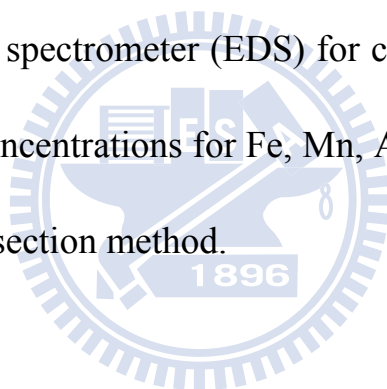
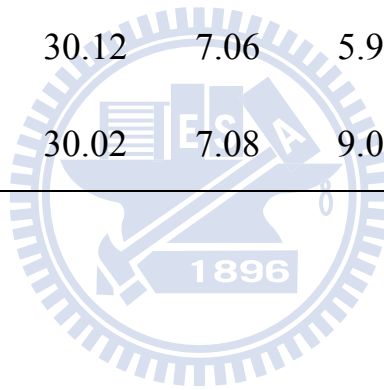


Table 3.1 Chemical compositions of the present alloys (wt.%).

Alloy	Mn	Al	Cr	C	Fe
A(0Cr)	29.18	7.05	0	0.96	Bal.
B(3Cr)	29.92	7.12	3.01	1.04	Bal.
C(6Cr)	30.12	7.06	5.96	1.01	Bal.
D(9Cr)	30.02	7.08	9.05	0.98	Bal.





### **3-3 Results and discussion**

Optical microscopy examinations showed that the as-quenched microstructure of the alloys A(0Cr) through C(6Cr) was single-phase austenite. Figure 3.1(a) shows a typical optical micrograph of the alloy C(6Cr), indicating single-phase austenite with annealing twins. Transmission electron microscopy examinations indicated that besides the austenite phase, no evidence of carbides could be detected in the as-quenched alloys A(0Cr) through C(6Cr). Figure 3.1(b) is an optical micrograph of the alloy D(9Cr), revealing the presence of some carbides in the austenite matrix and on the grain boundaries. It seems to imply that Cr could be completely dissolved in the austenite matrix at 1373K as  $\text{Cr} \leq 6$  wt.%, and carbides could be formed at this temperature as Cr up to 9 wt.%. Potentiodynamic polarization curves for the four Fe-Mn-Al-Cr-C alloys in 3.5% NaCl solution are shown in Figure 3.2. The electrochemical parameters are summarized in Table 3.2.  $E_{\text{corr}}$  of the alloys with different Cr content was varied from -556 mV to -877 mV. Alloy C(6Cr) has the noblest  $E_{\text{corr}}$  (-556mV). Similarly, with increasing Cr content from 3 to 6 wt%, the  $E_{\text{pp}}$  was drastically increased from -224mV to -27mV. However, with further increasing the Cr content to 9 wt%,  $E_{\text{pp}}$  became more negative (-472mV). The results indicate that the alloy C(6Cr) had the highest resistivity to pitting damage. Passivation could be observed for all the alloys except for the alloy without Cr content. In Figure

3.2, it is clearly seen that the passive region increased as Cr content increased from 0 to 6 wt.%, and decreased as Cr content up to 9 wt.%. In order to determine the chemical composition and the valence state of element in passive film formed on the alloys in 3.5% NaCl solution, the technique of AES/XPS was undertaken. Figure 3.3 indicates that the depth-concentration profiles for passive film formed on the alloys A(0Cr), C(6Cr) and D(9Cr). The detection of carbon concentration of outmost layer may be due to surface contamination. The O concentration of the alloy A(0Cr) was much smaller than that of the alloys C(6Cr) and D(9Cr) in depth profile. In Figure 3.3(a), it is clear that passive film was not obvious in the alloy without Cr content. However, in the alloys C(6Cr) and D(9Cr), the O concentration at the surface was much higher than that in the matrix, as illustrated in Figures 3.3(b) and (c). The Mn and Fe contents in the outmost surface were much lower than those in the matrix, but Cr and Al contents were reverse tendency. It means that the Cr and Al enrichment was attributed to the preferential dissolution of unstable oxides of Fe and Mn into electrolyte solution, and then replacement by Cr and Al within the oxide layer. There were broad peaks of Cr and Al at a depth of 0 to 2nm, which corresponded with the peak of O. This implies that the increase of Cr and Al in oxides is likely to be responsible for the improved stability of the passive film. However, the AES analysis for passive film can not explain the reason why the

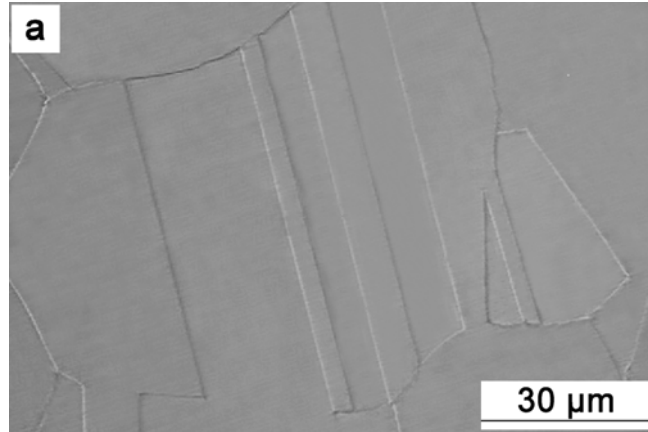


Figure 3.1 (a)

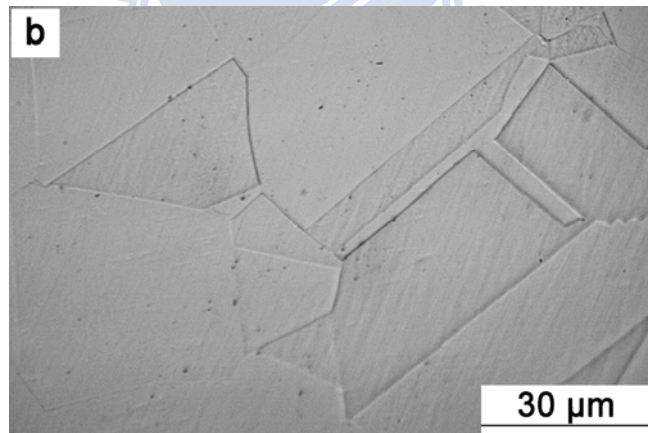


Figure 3.1 (b)

Figure 3.1 Optical micrographs of the Fe-30wt.%Mn-7wt.%Al-(6, 9)wt.% Cr-1wt.%C alloys. (a) 6 wt.%Cr, and (b) 9 wt.%Cr.

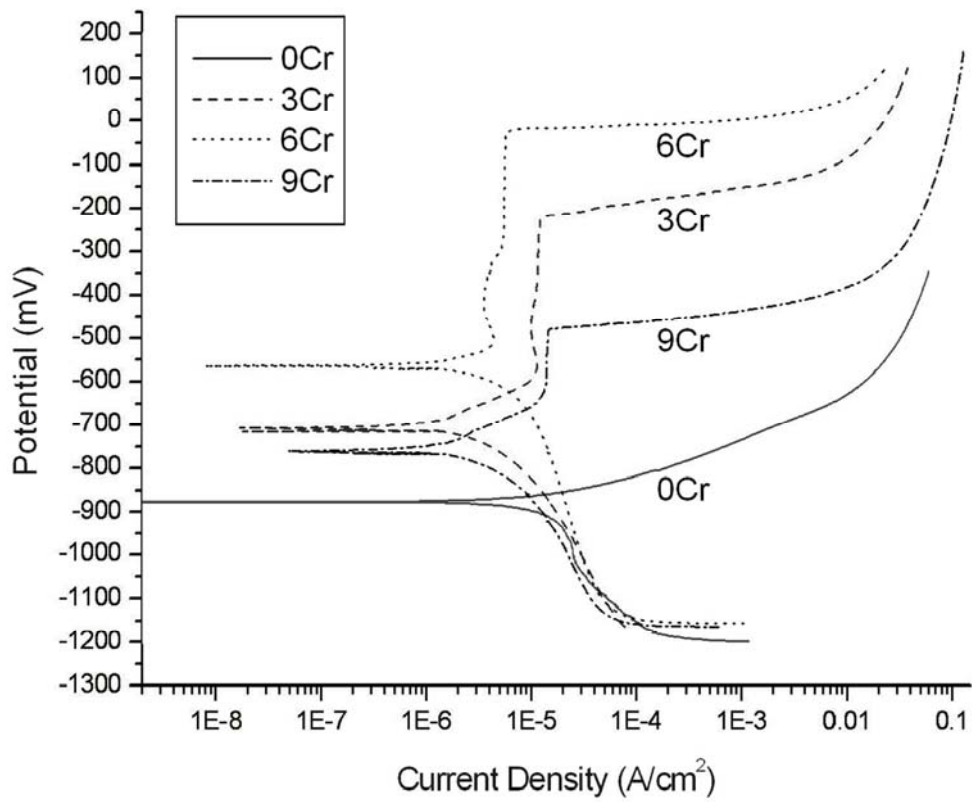


Figure 3.2 Potentiodynamic polarization curves for the five Fe-30wt.%Mn-7wt.%Al-(0, 3, 6, and 9)wt.%Cr-1wt.%C alloys in 3.5% NaCl solution.

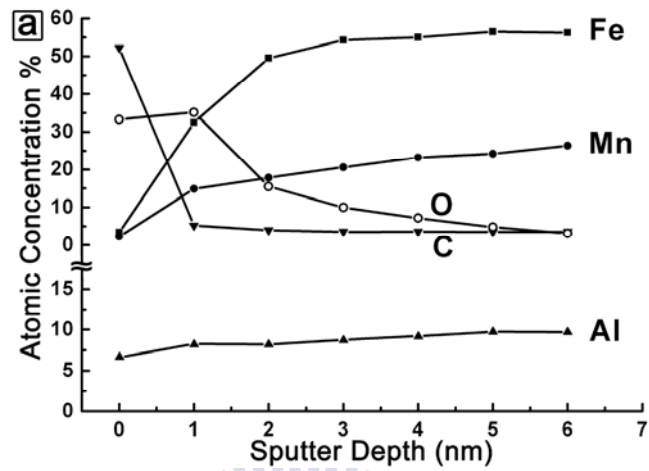


Figure 3.3 (a)

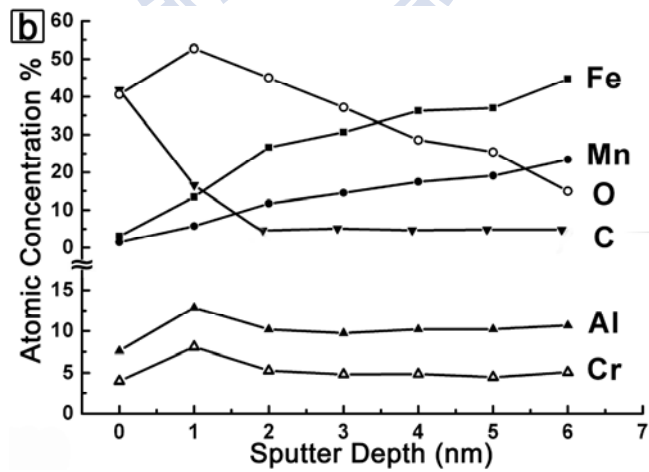


Figure 3.3 (b)

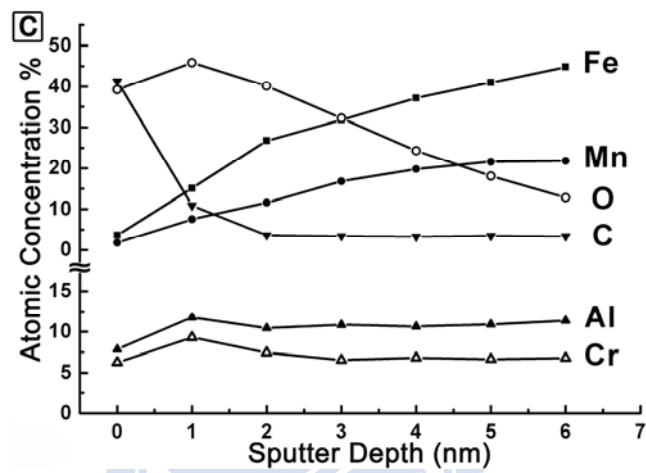


Figure 3.3 (c)

Figure 3.3 AES depth profiles for the passive film of the Fe-30wt.%Mn-7wt.%Al-(0, 6, and 9)wt.%Cr-1wt.%C alloys. (a) 0 wt.%Cr, (b) 6 wt.%Cr, and (c) 9 wt.%Cr.

Table 3.2 The electrochemical parameters from potentiodynamic polarization curves for the Fe-30wt.%Mn-7wt.%Al-(0, 3, 6 and 9)wt.%Cr-1wt.%C alloys in 3.5% NaCl solution.<sup>(\*)</sup>

Alloy	Electrochemical Parameters from Polarization Curves			
	E <sub>corr</sub> (mV)	E <sub>cr</sub> (mV)	E <sub>pp</sub> (mV)	I <sub>p</sub> (A/cm <sup>2</sup> )
A(0Cr)	-877	--	--	--
B(3Cr)	-712	-588	-224	4.1E-05
C(6Cr)	-556	-518	-27	5.75E-06
D(9Cr)	-754	-599	-472	1.78E-05

<sup>(\*)</sup>E<sub>corr</sub>, corrosion potential; E<sub>cr</sub>, critical potential for active-passive transition; E<sub>pp</sub>, pitting potential; I<sub>p</sub>, passive current density, minimum value.

$E_{\text{corr}}$  of the alloy D(9Cr) decreased (more negative), as indicated in Table 3.2. In order to obtain more information, the alloy with 9 wt.% Cr content was examined by TEM. Figure 3.4(a), a bright-field electron micrograph, clearly reveals the presence of carbides in the austenite matrix. Figure 3.4(b) is a selected-area diffraction pattern taken from a carbide. Compared to the previous studies [20], it is clear that the carbide is  $(\text{Fe},\text{Mn},\text{Cr})_7\text{C}_3$  with lattice parameters  $a = 1.398\text{nm}$  and  $c = 0.452\text{nm}$ . Figures 3.4(c) and (d) are two EDS profiles taken from a  $(\text{Fe},\text{Mn},\text{Cr})_7\text{C}_3$  carbide and the austenite matrix nearby the  $(\text{Fe},\text{Mn},\text{Cr})_7\text{C}_3$  carbide, respectively. The quantitative analyses of ten different EDS profiles showed that the chemical composition of the carbide was Fe-0.56wt.%Al-40.12wt.%Mn-34.39wt.%Cr (EDS with the thick-window detector can only detect the elements with atomic number 11 or above, hence carbon is unable to be examined by this method), and the chemical composition of the austenite matrix nearby the carbide was Fe-10.51wt.%Al-25.48wt.%Mn-2.73wt.%Cr. It is clearly seen that the Cr content in the  $(\text{Fe},\text{Mn},\text{Cr})_7\text{C}_3$  carbide is up to 34.39wt.%, which is much higher than that in the austenite matrix nearby the  $(\text{Fe},\text{Mn},\text{Cr})_7\text{C}_3$  carbide. It is thus expected that the conspicuous decrease of the Cr content in the austenite matrix was ascribed to the formation of Cr-rich  $(\text{Fe},\text{Mn},\text{Cr})_7\text{C}_3$  carbides. Therefore, it is deduced that the formation of Cr-rich  $(\text{Fe},\text{Mn},\text{Cr})_7\text{C}_3$  carbides would lead to the decrease of  $E_{\text{corr}}$  and  $E_{\text{pp}}$  of the alloy D(9Cr).



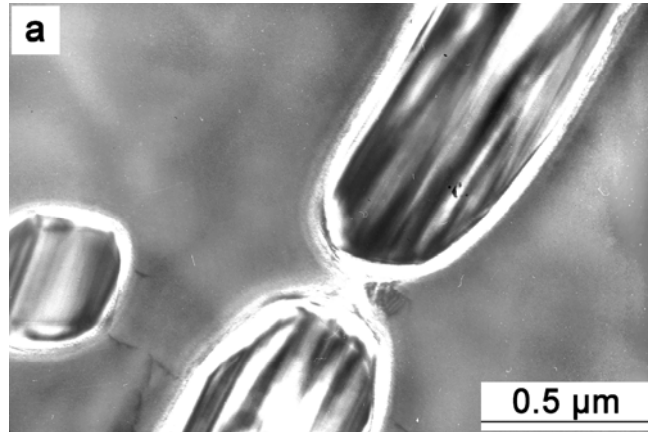


Figure 3.4 (a)



Figure 3.4 (b)

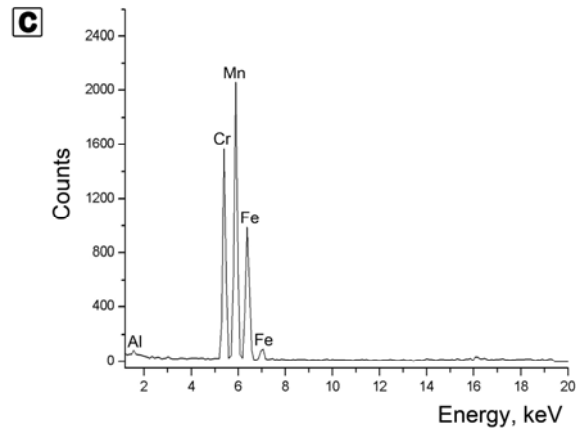


Figure 3.4 (c)

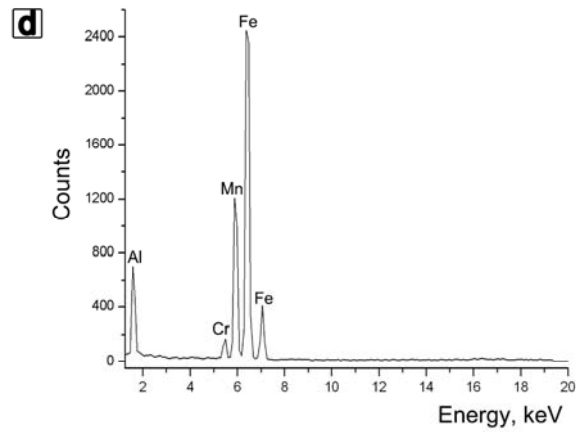


Figure 3.4 (d)

Figure 3.4 Transmission electron micrographs of the Fe-30wt.%Mn-7wt.%Al-9wt.%Cr-1wt.%C alloy. (a) BF, and (b) a selected-area diffraction pattern taken from a  $(\text{Fe,Mn,Cr})_7\text{C}_3$  carbide in (a). The zone axis of the  $(\text{Fe,Mn,Cr})_7\text{C}_3$  carbide is  $[\bar{1}2\bar{1}0]$ . (c) and (d) two typical EDS profiles obtained from the  $(\text{Fe,Mn,Cr})_7\text{C}_3$  carbide and the  $\gamma$  matrix nearby the  $(\text{Fe,Mn,Cr})_7\text{C}_3$  carbide, respectively.

Based on the preceding results, it is clear that no evidence of passivation could be found in the alloy A(0Cr) and the  $E_{\text{corr}}$  of the alloy was -877mV. This result is similar to that examined by other workers in the as-quenched austenitic Fe-(26.0-32.2)wt.%Mn-(8.3-10.0)wt.%Al-(0.85-1.45)wt.%C alloys in 3.5% NaCl solution, in which they reported that only narrow passive region could be observed and the  $E_{\text{corr}}$  of the alloys was in the range from -789 to -920 mV [5-9,14]. However, an obvious broad passive region could be detected in the present alloys containing Cr. This shows that the Cr addition is indeed beneficial for the corrosion resistance of the austenitic Fe-Mn-Al-C alloys in NaCl solution, which is in agreement with that examined by other workers in the austenitic Fe-(29.5-31.3)wt.%Mn-(8.4-8.9)wt.%Al-(2.6-2.8)wt.%Cr-(0.98-1.06)wt.%C alloys [5,6]. In addition, the  $E_{\text{corr}}$  value for the alloy B(3Cr) was -712 mV, which is comparable to about -720 mV for the as-quenched Fe-29.5wt.%Mn-8.4wt.%Al-2.6wt.%Cr-1.06wt.%C alloy in 3.5% NaCl solution reported by other workers [6]. In the present study, we have further shown that the 6.0 wt.% Cr addition was completely dissolved in the Fe-30wt.%Mn-7wt.%Al-1.0wt.%C alloy at 1373K. Thus, the  $E_{\text{corr}}$  and  $E_{\text{pp}}$  values would be pronouncedly increased to -556 mV and -27mV, respectively, in the alloy C(6Cr). However, when the Cr addition was increased up to 9 wt%, the Cr-rich  $(\text{Fe,Mn,Cr})_7\text{C}_3$  carbides could be detected in the as-quenched alloy D(9Cr). The formation of Cr-rich

$(\text{Fe,Mn,Cr})_7\text{C}_3$  carbides resulted in the drastic decrease of the  $E_{\text{corr}}$  and  $E_{\text{pp}}$  values.



### **3-4 Conclusions**

The corrosion potential ( $E_{\text{corr}}$ ) of the as-quenched Fe-30wt.%Mn-7wt.%Al- (0, 3, 6 and 9)wt.%Cr-1wt.%C alloys increased from -877 mV to -556 mV as Cr content increased from 0 to 6 wt.%. However, the  $E_{\text{corr}}$  of the alloy with 9 wt.% Cr dropped to -754 mV due to the formation of  $(\text{Fe,Mn,Cr})_7\text{C}_3$  carbides in the austenitic matrix and on the grain boundaries. The result indicates that the alloy C (6Cr) exhibited the highest corrosion resistance in 3.5% NaCl solution. Passivation could be observed for all of the present alloys except for the alloy without Cr content.



## References

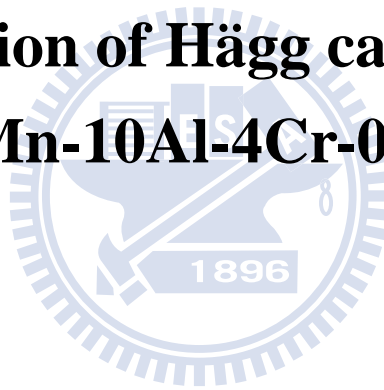
1. Zhu SM, Tjong SC, *Metalls. Trans. A* 29 (1998) 299.
2. Choo WK, Kim JH, Yooh JC, *Acta Mater.* 45 (1997) 4877.
3. Kalashnikov IS, Acselrad O, Pereira LC, Kalichak T, Khadyev MS, *Journal of Materials Engineering and Performance* 9 (2000) 334.
4. Chang SC, Hsiau YH, *J. Mater. Sci.* 24 (1989) 1117.
5. Chang SC, Liu JY, Juang HK, *Corrosion. Eng.* 51 (1995) 399.
6. Chang SC, Weng WH, Chen HC, Lin SJ, Chung PCK, *Wear* 181-183 (1995) 511.
7. Tsai WT, Duh JB, Lee JT, *J. Mater. Sci.* 22 (1987) 3517.
8. Duh JB, Tsai WT, Lee JT, *Corrosion Nov* (1988) 810.
9. Ruscak M, Perng TP, *Corrosion Oct* (1995) 738.
10. Tjong SC, Wu CS, *Mater. Sci. Eng.* 80 (1986) 203.
11. Tjong SC, *Surface and Coatings Technology* 28 (1986) 181.
12. Wang CJ, Chang YC, *Mater. Chem. Phy.* 76 (2002) 151.
13. Zhu XM, Zhang YS, *Corrosion* 54 (1998) 3.
14. Shih ST, Tai CY, Perng TP, *Corrosion Feb* (1993) 130.
15. Tsu IF, Perng TP, *Metall. Trans. A* 22 (1991) 215.
16. Wu CC, Chou JS, Liu TF, *Metall. Trans. A* 22 (1991) 2265.
17. Zhu SM, Tjong SC, *Scripta* 36 (1997) 317.

18. J.M. Walls, *Methods of Surface Analysis*, Cambridge University Press, New York, 1989.
19. David Briggs, John T, Grant (Ed.), *Surface Analysis by Auger and X-Ray*
20. Ernst F, Cao Y, Michal GM, *Acta Materialia* 52 (2004) 1469.



# **Chapter 4.**

## **Formation of Hägg carbide in an Fe-30Mn-10Al-4Cr-0.45C alloy**

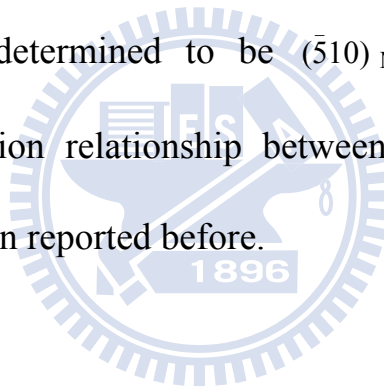




# Formation of Hägg carbide in an Fe-30Mn-10Al-4Cr-0.45C alloy

## Abstract

When the present alloy was aged at 550°C, Hägg carbides ( $M_5C_2$ -type carbides) occurred at  $a/2 \langle 100 \rangle$  anti-phase boundaries of the  $D0_3$  domains. The Hägg carbide has never been observed by previous workers in FeMnAlC and FeMnAlCrC alloy systems. The orientation relationship between Hägg carbide and  $D0_3$  matrix was determined to be  $(\bar{5}10)_{M_5C_2} // (1\bar{1}0)_{D0_3}$  and  $(13\bar{4})_{M_5C_2} // (10\bar{2})_{D0_3}$ . The orientation relationship between Hägg carbide and bcc-type phase has also never been reported before.



## **4-1 Introduction**

In previous studies [1-6], it is seen that the as-quenched microstructure of the Fe-(28-34)wt.%Mn-(7.8-11)wt.%Al-(0.54-1.3)wt.%C alloys was single-phase austenite ( $\gamma$ ). After being aged at 500~750°C for moderate times, fine and coarse (Fe,Mn)<sub>3</sub>AlC carbides were found to precipitate coherently within the  $\gamma$  matrix and heterogeneously on the  $\gamma/\gamma$  grain boundaries, respectively. For convenience, the  $\kappa'$  carbide and  $\kappa$  carbide were used to represent the (Fe,Mn)<sub>3</sub>AlC carbide formed coherently within the  $\gamma$  matrix and heterogeneously on the  $\gamma/\gamma$  grain boundaries [2]. After prolonged aging time within this temperature range, the coarse  $\kappa$  carbides grew into adjacent  $\gamma$  grains through a  $\gamma \rightarrow \alpha$  (ferrite) +  $\beta$ -Mn reaction, a  $\gamma \rightarrow \gamma_0$  (carbon-deficient austenite) +  $\kappa$  reaction, a  $\gamma \rightarrow \beta$ -Mn +  $\kappa$  reaction or a  $\gamma \rightarrow \alpha + \beta$ -Mn +  $\kappa$  reaction [1-5], depending on the chemical composition and aging temperature. In the FeMnAlC alloys with lower carbon content (i.e. 0.4~0.51wt.%C), the as-quenched microstructure was found to be ( $\gamma+\alpha$ ) dual phases [7-9]. After being aged at 550~710°C, fine  $\kappa'$  carbides were found to appear within the  $\gamma$  grains, and coarse  $\kappa$  carbides as well as  $\beta$ -Mn precipitates could be observed in the  $\alpha$  grains and on the  $\alpha/\alpha$  grain boundaries [8, 9]. In 1991, the present workers examined the microstructural developments of an Fe-28.6wt.%Mn-10.1wt.%Al-0.46wt.%C alloy [10]. Consequently, it was found that in the as-quenched condition,

extremely fine  $D0_3$  domains could be observed within the  $\alpha$  grains. This is different from that reported by other workers in the duplex FeMnAlC alloys. When the alloy was aged at temperatures ranging from  $450^\circ\text{C}$  to  $750^\circ\text{C}$ , the phase transformation sequence occurring within the  $\alpha$  grain was found to be  $\alpha + D0_3 \rightarrow \alpha + D0_3 + \kappa \rightarrow \alpha + B2 + \kappa \rightarrow \alpha$  [10].

In order to improve the corrosion resistance and high-temperature oxidation resistance, the Cr has been added to the austenitic or duplex FeMnAlC alloys [11-15]. Based on these results, it can be generally concluded that the addition of Cr does achieve these results. Additionally, the effects of Cr addition on the microstructures of the austenitic FeMnAlC alloys have also been examined by several researchers [16-17]. In the previous study [16], it is seen that when the Fe-30wt.%Mn-9wt.%Al-5wt.%Cr-0.7wt.%C alloy was aged at  $550\sim 750^\circ\text{C}$ , the fine  $\kappa'$  carbides were formed within the  $\gamma$  grain, and a  $(M_7C_3 + D0_3) \rightarrow (M_7C_3 + B2) \rightarrow (M_7C_3 + \alpha)$  reaction occurred on the  $\gamma/\gamma$  grain boundaries. Besides, when the Fe-28.3wt.%Mn-8.7wt.%Al-5.5wt.%Cr-1wt.%C alloy was aged at  $800\sim 1250^\circ\text{C}$ , a  $(\gamma + Cr_7C_3) \rightarrow \gamma \rightarrow (\gamma + (\alpha + B2 + D0_3))$  reaction occurred within the  $\gamma$  grain and on the  $\gamma/\gamma$  grain boundaries [17]. In contrast to the studies of the austenitic FeMnAlCrC alloys, information concerning the microstructures of the  $(\gamma+\alpha)$  duplex FeMnAlCrC alloys is very deficient. Therefore, the purpose of this work is an attempt to study the microstructural developments in the

Fe-30wt.%Mn-10wt.%Al-4wt.%Cr-0.45 wt.%C alloy aged at 550°C.



## **4-2 Experimental procedure**

The Fe-30wt.%Mn-10wt.%Al-4wt.%Cr-0.45wt.%C alloy was prepared in a vacuum induction furnace using pure Fe, Mn, Al, Cr and carbon powder. After being homogenized at 1250°C for 12 h, the ingot was hot-rolled to a final thickness of 2.0 mm. The sheet was subsequently solution heat-treated (SHT) at 1050°C for 1 h and then rapidly quenched into room-temperature water. Aging process was performed at 550°C for 12 h in a vacuum furnace followed by rapid quenching. Electron microscopy specimens were prepared by means of a double-jet electropolisher with an electrolyte of 65% ethanol, 20% acetic acid and 15% perchloric acid. Electron microscopy was performed on a JEOL 2100 transmission electron microscope (TEM) operating at 200kV. This microscope was equipped with a Link ISIS 300 energy-dispersive X-ray spectrometer (EDS) for chemical analysis. Quantitative analyses of elemental concentrations for Fe, Mn, Al and Cr were made using the Cliff-Lorimer ratio thin section method. The EDS with a thick-window detector is limited to detect the elements of atomic number of 11 or above. Therefore, carbon cannot be examined by this method.

### **4-3 Results and discussion**

In the as-quenched condition, the microstructure of the alloy was ( $\gamma+\alpha$ ) dual phases. No precipitates could be detected within the  $\gamma$  grains; however, extremely fine  $D0_3$  domains could be observed within the  $\alpha$  grains. The extremely fine  $D0_3$  domains were formed within the  $\alpha$  grains by a continuous ordering transition during quenching. This is similar to that observed by the present workers in the Fe-28.6wt.%Mn-10.1 wt.%Al-0.46 wt.%C alloy [10].

When the as-quenched alloy was aged at 550°C for 12 h, fine k' carbides were formed within the  $\gamma$  grain, as shown in Figure 4.1(a). Figure 4.2(a) is a bright-field (BF) electron micrograph taken from the  $\alpha$  grain, indicating that a lot of small precipitates occurred within the  $\alpha$  matrix. Figure 4.2(b) is a selected-area diffraction pattern (SADP) taken from the  $\alpha$  matrix, exhibiting the presence of the superlattice reflection spots of the ordered  $D0_3$  phase [10].

Figures 4.2(c) and (d) are the (111) and (200)  $D0_3$  dark-field (DF) electron micrographs taken from the same area as Figure 4.2(a), clearly revealing that the (111) DF image and the (200) DF image are morphologically identical. Therefore, the bright domains presented in Figures 4.2(c) and (d) are of the  $D0_3$  phase with  $a/2 \langle 100 \rangle$  anti-phase boundaries (APBs) [10]. Figure 4.2(e) is the DF image of the small precipitates, indicating that these precipitates have occurred preferentially at  $a/2 \langle 100 \rangle$  APBs of the  $D0_3$  domains. A preliminary

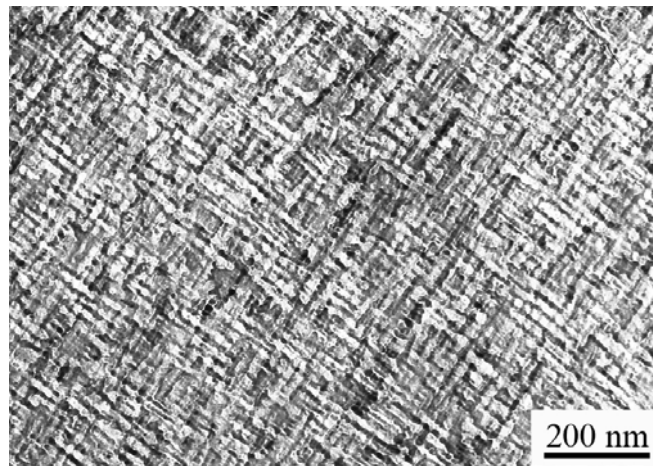


Figure 4.1 BF transmission electron micrograph taken from the  $\gamma$  matrix of the alloy aged at 550°C for 12 h.

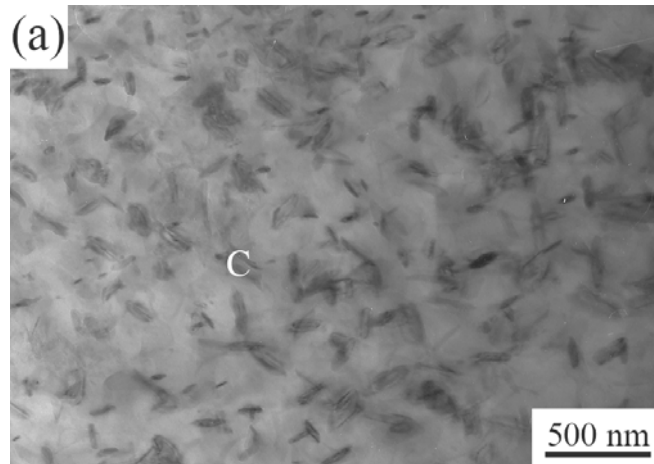


Figure 4.2 (a)

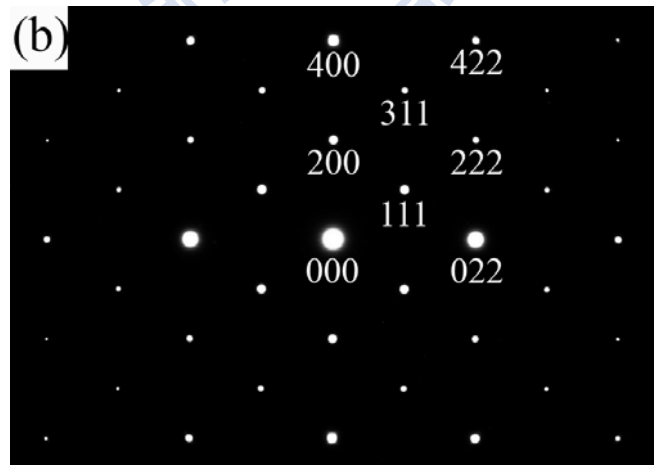


Figure 4.2 (b)



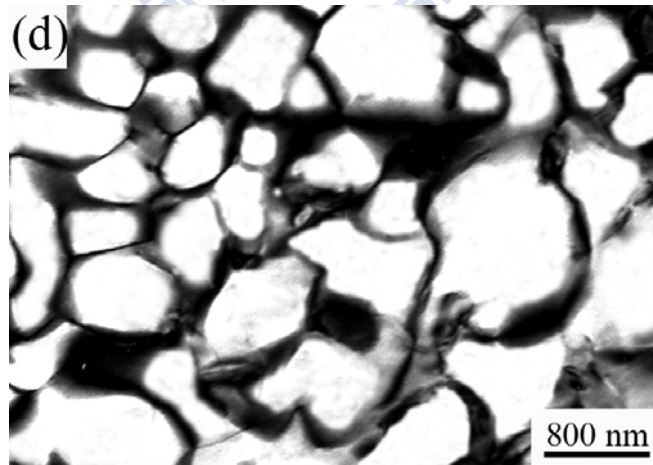
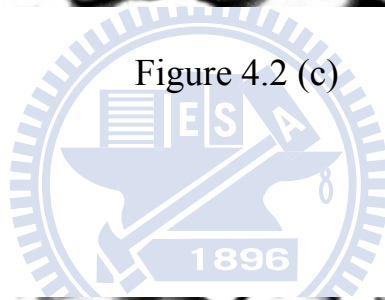
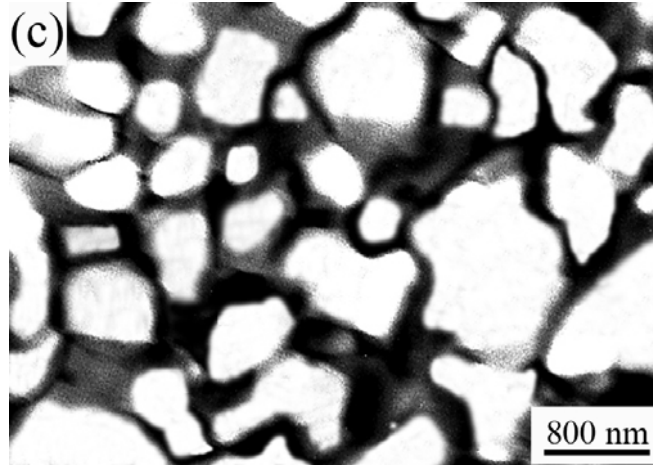


Figure 4.2 (d)

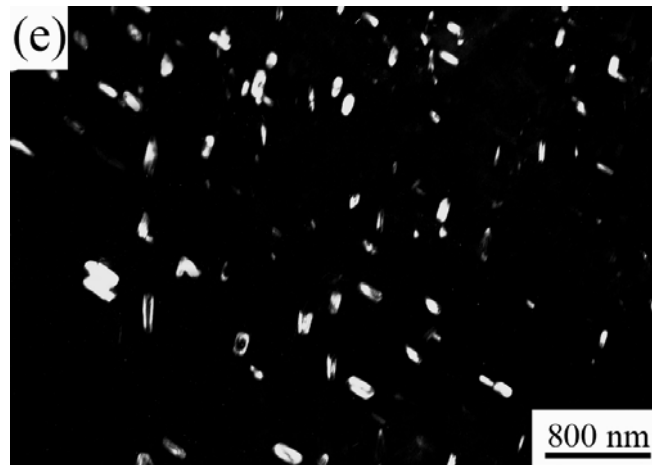


Figure 4.2 (e)

Figure 4.2 Transmission electron micrographs taken from the  $D0_3$  matrix of the alloy aged at  $550^\circ\text{C}$  for 12 h. (a) BF, (b) an SADP, the zone axis is  $[01\bar{1}]$ , (c) and (d)  $(111)$  and  $(200)$   $D0_3$  DF image, respectively, (e)  $(001)_{M_5C_2}$  DF image.

study of electron diffraction indicated that the precipitate was not of any known phases reported in FeMnAl, FeMnAlC and FeMnAlCrC alloy systems [1-17]. In order to clarify the crystal structure of the precipitate, eight SADPs taken from the precipitate marked as C in Figure 4.2(a) were obtained by tilting the specimen about some specific reflections. The results are shown in Figures 4.3(a)~(h). Table 4.1 shows the interplanar spacings of the precipitate phase, which were measured directly from the SADPs in Figures 4.3(a)~(h). The measured angles among the reciprocal lattice vectors are listed in Table 4.2. Using these measured values of the interplanar spacings and angles, the crystal structure of the precipitate was determined to be monoclinic with lattice parameters  $a=1.158\text{nm}$ ,  $b=0.452\text{nm}$ ,  $c=0.509\text{nm}$ , and  $\beta=98.3^\circ$ . Based on these lattice parameters, the interplanar spacings and the angles between the chosen reciprocal reflections were calculated by using the following equations [18]:

$$\frac{1}{d^2} = \frac{1}{a^2} \frac{h^2}{\sin^2 \beta} + \frac{1}{b^2} k^2 + \frac{1}{c^2} \frac{l^2}{\sin^2 \beta} - \frac{2hl \cos \beta}{ac \sin^2 \beta}$$

$$\cos \phi = \frac{\frac{1}{a^2} h_1 h_2 + \frac{1}{b^2} k_1 k_2 \sin^2 \beta + \frac{1}{c^2} l_1 l_2 - \frac{1}{ac} (l_1 h_2 + l_2 h_1) \cos \beta}{\left\{ \left( \frac{1}{a^2} h_1^2 + \frac{1}{b^2} k_1^2 \sin^2 \beta + \frac{1}{c^2} l_1^2 - \frac{2h_1 l_1}{ac} \cos \beta \right) \times \left( \frac{1}{a^2} h_2^2 + \frac{1}{b^2} k_2^2 \sin^2 \beta + \frac{1}{c^2} l_2^2 - \frac{2h_2 l_2}{ac} \cos \beta \right) \right\}^{1/2}}$$

The calculated interplanar spacings and angles are also listed in Table 4.1 and Table 4.2 for comparison. It is seen in Table 4.1 and Table 4.2 that the

measured values are quite consistent with those obtained by calculation. Therefore, the SADPs of the precipitate phase in Figures 4.3(a)~(h) could all be indexed. The zone axes of Figures 4.3(a)~(h) are  $[110]$ ,  $[210]$ ,  $[1\bar{1}0]$ ,  $[3\bar{1}\bar{2}]$ ,  $[10\bar{1}]$ ,  $[31\bar{4}]$ ,  $[11\bar{2}]$  and  $[22\bar{3}]$ , respectively. Compared with previous studies [19-23], it is clear that the crystal structure of the precipitate corresponds to that of the Hägg carbide ( $M_5C_2$ -type carbide).

Based on the preceding observations, two important experimental results are discussed below. ( I ) The coarse Mn-rich  $\kappa$  carbides or Mn-rich  $\beta$ -Mn precipitates were always observed within the  $\alpha$  or  $D0_3$  matrix in the duplex FeMnAlC alloys aged at  $450\sim 750^\circ\text{C}$  [8-10]. However, only  $M_5C_2$  carbides were formed at  $a/2\langle 100\rangle$  APBs of the well-grown  $D0_3$  domains, and no evidence of  $\kappa$  carbide or  $\beta$ -Mn precipitate could be detected within the  $\alpha$  grain in the present alloy aged at  $550^\circ\text{C}$ . In order to clarify the apparent difference, an TEM-EDS study was made. The average concentrations of the alloying elements were obtained from at least ten different EDS profiles of each phase. The results are summarized in Table 4.3. It is seen in Table 4.3 that the Cr and Mn concentrations in the well-grown  $D0_3$  domains were much lower than those in the as-quenched alloy, and the reverse result was obtained in the  $M_5C_2$  carbide. Therefore, it is believed that during the growth of the  $D0_3$  domains, partial Cr and Mn atoms would proceed to diffuse toward the  $a/2\langle 100\rangle$  APBs. The

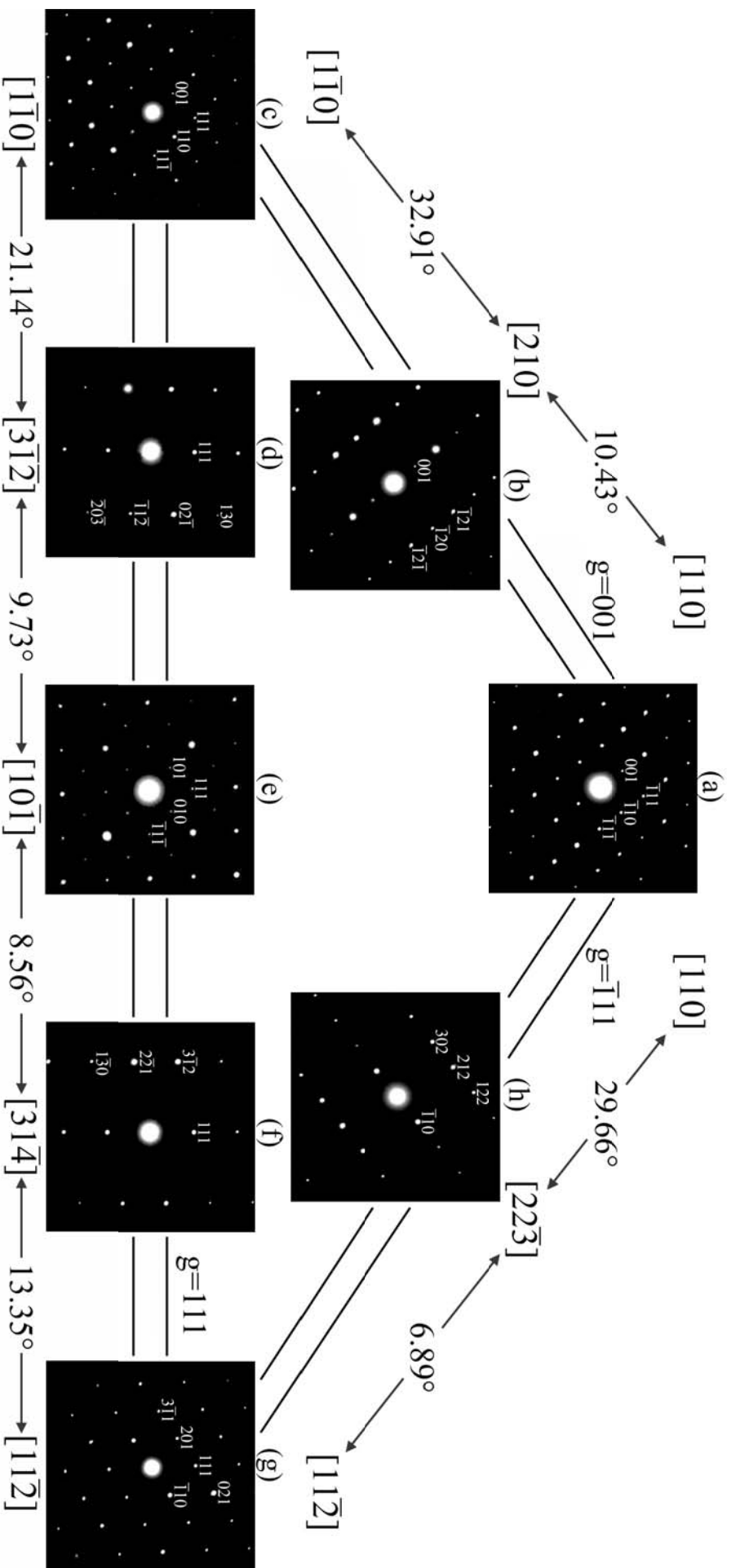


Figure 4.3 Eight SADPs taken from the precipitate marked “C” in Figure 4.2(a). The zone axes are (a)  $[110]$ , (b)  $[210]$ , (c)  $[1\bar{1}0]$ , (d)  $[3\bar{1}2]$ , (e)  $[10\bar{1}]$ , (f)  $[31\bar{4}]$ , (g)  $[11\bar{2}]$  and

(h)  $[22\bar{3}]$ , respectively.

Table 4.1 The d-spacings of the Hägg carbide.

	Observed d-spacing*	Calculated d-spacing**	Indexed Plane
1	0.504	0.504	001
2	0.452	0.452	010
3	0.437	0.438	101
4	0.418	0.420	$\bar{1}10$
5	0.419	0.420	110
6	0.315	0.315	111
7	0.331	0.332	$\bar{1}11$
8	0.330	0.332	$11\bar{1}$
9	0.316	0.315	$1\bar{1}1$
10	0.208	0.206	$02\bar{1}$
11	0.220	0.222	$\bar{1}20$
12	0.352	0.354	201
13	0.411	0.409	$20\bar{1}$
14	0.213	0.211	$\bar{1}1\bar{2}$
15	0.206	0.205	$\bar{1}21$
16	0.203	0.201	$\bar{1}2\bar{1}$
17	0.367	0.364	122
18	0.195	0.197	212
19	0.193	0.190	$2\bar{2}1$
20	0.145	0.149	$1\bar{3}0$
21	0.238	0.241	$3\bar{1}1$
22	0.159	0.155	$20\bar{3}$
23	0.197	0.198	302
24	0.180	0.181	$3\bar{1}2$
25	0.268	0.266	$40\bar{1}$
26	0.099	0.097	$13\bar{4}$
27	2.048	2.044	$\bar{5}10$

\*The observed d-spacings were measured from SADPs,

\*\*The calculated d-spacings were obtained on the basis of the monoclinic structure with lattice parameters  $a=1.158\text{nm}$ ,  $b=0.452\text{nm}$ ,  $c=0.509\text{nm}$  and  $\beta=98.3\text{ deg}$ .

Table 4.2 Angles among some reciprocal vectors of the Hägg carbide.

	Two Desired Reciprocal Vectors	Observed Angle*	Calculated Angle**
Fig. 3(a)	(001) and ( $\bar{1}11$ )	51.8	51.9
	(001) and ( $\bar{1}10$ )	93.1	93.0
	(001) and ( $\bar{1}1\bar{1}$ )	131.5	131.6
Fig. 3(b)	(001) and ( $\bar{1}21$ )	67.5	67.6
	(001) and ( $\bar{1}20$ )	91.4	91.6
	(001) and ( $\bar{1}2\bar{1}$ )	115.0	115.1
Fig. 3(c)	(001) and (111)	48.5	48.4
	(001) and (110)	87.0	87.0
	(001) and (11 $\bar{1}$ )	128.3	128.1
Fig. 3(d)	(111) and (02 $\bar{1}$ )	68.5	68.7
	(111) and ( $\bar{1}1\bar{2}$ )	107.5	107.4
	(111) and ( $\bar{2}0\bar{3}$ )	135.7	135.5
Fig. 3(e)	(111) and (101)	44.3	44.1
	(111) and (010)	45.8	45.9
	(111) and ( $\bar{1}1\bar{1}$ )	91.6	91.8
Fig. 3(f)	(111) and (3 $\bar{1}2$ )	68.3	68.2
	(111) and ( $\bar{2}2\bar{1}$ )	102.5	102.4
	(111) and (1 $\bar{3}0$ )	130.2	130.0
Fig. 3(g)	(111) and ( $\bar{1}10$ )	59.0	59.1
	(111) and (204)	45.3	45.1
	(111) and (3 $\bar{1}1$ )	79.6	79.8
Fig. 3(h)	( $\bar{1}10$ ) and (122)	53.8	53.9
	( $\bar{1}10$ ) and (212)	76.4	76.2
	( $\bar{1}10$ ) and (302)	103.5	103.4
Fig. 4(a)	(20 $\bar{1}$ ) and ( $\bar{3}1\bar{1}$ )	92.1	92.1
	(20 $\bar{1}$ ) and ( $\bar{5}10$ )	122.0	122.1
Fig. 4(b)	(20 $\bar{1}$ ) and (40 $\bar{1}$ )	89.5	89.3
	( $\bar{1}1\bar{1}$ ) and (13 $\bar{4}$ )	21.5	21.4
	( $\bar{1}1\bar{1}$ ) and ( $\bar{5}10$ )	50.3	50.2

\*The observed angles were measured from SADPs

\*\*The calculated angles were obtained on the basis of the monoclinic structure with lattice parameters  $a=1.158\text{nm}$ ,  $b=0.452\text{nm}$ ,  $c=0.509\text{nm}$  and  $\beta=98.3$  deg.

Table 4.3 Chemical compositions of the phases revealed by EDS.

Heat Treatment	Phase	Chemical Composition (at.%)			
		Fe	Mn	Al	Cr
SHT	$\gamma$	49.07	30.20	17.05	3.68
	$\alpha + D0_3$	52.07	21.80	21.55	4.58
550°C, 12h	$D0_3$	57.56	16.32	25.18	0.94
	$M_5C_2$	30.56	43.20	1.02	25.22



higher concentrations of both Cr and Mn would cause the (Cr,Mn)-rich  $M_5C_2$  carbides to precipitate at  $a/2 \langle 100 \rangle$  APBs. The precipitation of the (Cr,Mn)-rich  $M_5C_2$  carbides would decrease the Mn concentration drastically, thus inhibiting the precipitation of both Mn-rich  $\kappa$  carbides and Mn-rich  $\beta$ -Mn precipitates within the  $\alpha$  grain. ( II ) The Hägg carbide was extensively observed by many workers in the bcc-type alloys [20-24]. Depending on the chemical compositions, the lattice parameters of the Hägg carbide varied in the range of  $a=1.150-1.158\text{nm}$ ,  $b=0.452-0.457\text{nm}$ ,  $c=0.501-0.509\text{nm}$  and  $\beta=97.6-98.3^\circ$  [19-22]. However, to date, the orientation relationship between the Hägg carbide and the bcc-type (i.e.  $\alpha$ ,  $D0_3$ , B2) structure is very deficient. We are aware of two articles [22, 23], in which they reported that both  $Fe_5C_2$  carbide and  $Fe_3C$  carbide were formed intimately in  $\alpha$ -iron after being heat-treated at  $500-800^\circ\text{C}$  under a CO or/and  $H_2$  atmosphere. By using electron diffraction, the orientation relationship between the  $Fe_5C_2$  and  $Fe_3C$  was determined to be  $(100)_{Fe_5C_2} // (001)_{Fe_3C}$  [22, 23]. In addition, they correlated the obtained result with the orientation relationship between  $Fe_3C$  and  $\alpha$  phase,  $(001)_{Fe_3C} // (211)_\alpha$ , which was reported by other workers in ferritic stainless steel [24]. Therefore, they deduced that the orientation relationship among  $Fe_5C_2$ ,  $Fe_3C$  and  $\alpha$  phase was  $(100)_{Fe_5C_2} // (001)_{Fe_3C} // (211)_\alpha$  [23]. It is well-known that the orientation relationship between two phases should be described by a pair of parallel directions in a pair of

parallel planes or two pairs of parallel planes. However, in the previous studies [22 ,23], only a pair of parallel planes was determined and no direct experiment evidence confirmed the orientation relationship between  $\text{Fe}_5\text{C}_2$  and  $\alpha$  phase. Therefore, the electron diffraction technique was used to clarify the orientation relationship between the  $\text{M}_5\text{C}_2$  carbide and the  $\text{D0}_3$  matrix in the present study. The results are presented in Figures 4.4(a) and (b). In these two SADPs, it is clear that the  $(\bar{5}10)$  and  $(13\bar{4})$  reflection spots of the  $\text{M}_5\text{C}_2$  carbide are parallel to the  $(1\bar{1}0)$  and  $(\bar{1}02)$  reflection spots of the  $\text{D0}_3$  matrix, respectively. Accordingly, the orientation relationship between the  $\text{M}_5\text{C}_2$  carbide and  $\text{D0}_3$  matrix can be stated as follows:  $(\bar{5}10)_{\text{M}_5\text{C}_2} // (1\bar{1}0)_{\text{D0}_3}$  and  $(13\bar{4})_{\text{M}_5\text{C}_2} // (10\bar{2})_{\text{D0}_3}$ . In order to further certify the determined orientation relationship, the angle between the  $(\bar{5}10)_{\text{M}_5\text{C}_2}$  and  $(13\bar{4})_{\text{M}_5\text{C}_2}$  was calculated by using the equation mentioned above. The calculated angle was  $71.61^\circ$ , which is quite consistent with the angle of  $71.57^\circ$  between the  $(1\bar{1}0)_{\text{D0}_3}$  and  $(10\bar{2})_{\text{D0}_3}$ . Finally, it is worth mentioning that in the present study, a lot of effort was made to determine the parallel relationship of lower index planes between the  $\text{M}_5\text{C}_2$  carbide and  $\text{D0}_3$  matrix. Unfortunately, the attempt was not successful.

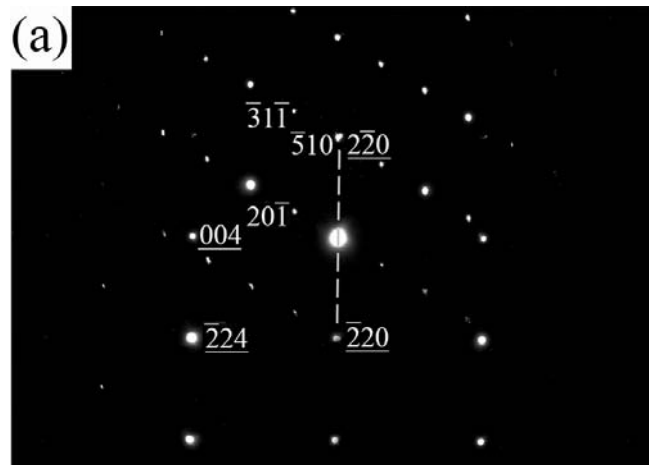


Figure 4.4 (a)

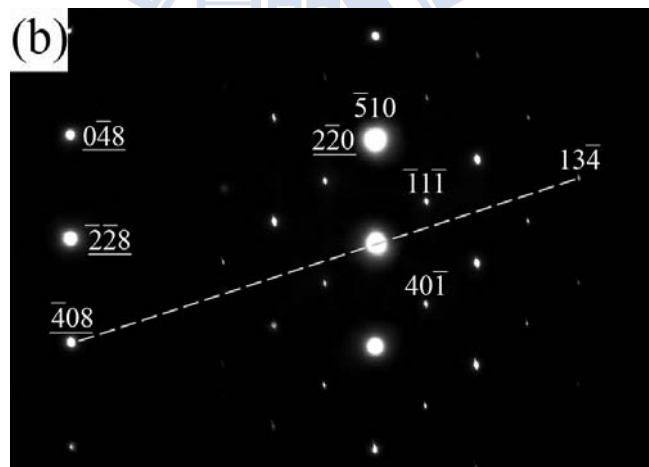


Figure 4.4 (b)

Figure 4.4 Two SADPs taken from an area including the precipitate marked “C” in Figure 4.2(a) and its surrounding matrix. The zone axes are (a)  $[152]_{M_5C_2}$ ,  $[110]_{D0_3}$  and (b)  $[154]_{M_5C_2}$ ,  $[221]_{D0_3}$ , respectively. ( $hkl=M_5C_2$  carbide;  $\underline{hkl}=D0_3$  phase)

## 4-4 Conclusions

In Summary, the as-quenched microstructure of the Fe-30wt.%Mn-10wt.%Al-4wt.%Cr-0.45wt.%C alloy was ( $\gamma+\alpha$ ) dual phases, and extremely fine  $D0_3$  domains could be observed within the  $\alpha$  grains. After being aged at 550°C for 12 h, fine  $\kappa'$  carbides were formed within the  $\gamma$  grains and the (Cr,Mn)-rich Hägg carbides occurred at  $a/2 \langle 100 \rangle$  APBs of the well-grown  $D0_3$  domains. The Hägg carbide has never been observed by previous workers in FeMnAlC and FeMnAlCrC alloy systems. The orientation relationship between the Hägg carbide and  $D0_3$  matrix was determined to be  $(\bar{5}10)_{M_5C_2} // (1\bar{1}0)_{D0_3}$  and  $(13\bar{4})_{M_5C_2} // (10\bar{2})_{D0_3}$ . The orientation relationship between Hägg carbide and bcc-type phase has also never been reported by other workers before.

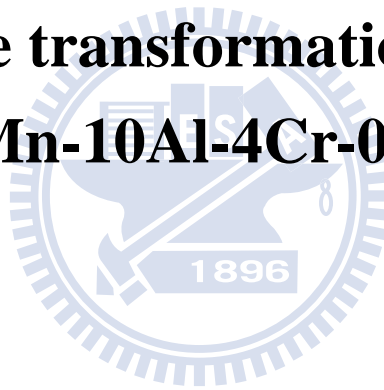
## References

1. K. Sato, K. Tagawa, Y. Inoue, Metall. Trans. A 21A (1990) 5.
2. W.K. Choo, J.H. Kim, J.C. Yoon, Acta Mater. 45 No.12 (1997) 4877.
3. C.Y. Chao, C.N. Hwang, T.F. Liu, Scripta Metall. 28 (1993) 109.
4. G.S. Krivonogov, M.F. Alekseyenko, G.G. Solovyeva, Fiz. Metal. Metalloved 39 No.4 (1975) 775.
5. C.N. Hwang, C.Y. Chao, T.F. Liu, Scripta Metall. 28 (1993) 263.
6. T.F. Liu, J.S. Chou, C.C. Wu, Metall. Trans. A 21A (1990) 1891.
7. S.C. Tjong, S.M. Zhu, Mater. Trans. 38 No.2 (1997) 112.
8. S.C. Tjong, N.J. Ho, Metallography 21 (1988) 199.
9. T.F. Liu, C.M. Wan, Strength Met. Alloys 1 (1986) 423.
10. C.C. Wu, J.S. Chou, T.F. Liu, Metall. Trans. A 22A (1991) 2265.
11. C.S. Wang, C.Y. Tsai, C.G. Chao, T.F. Liu, Mater. Trans. 48 (2007) 2973.
12. Y.H. Tuan, C.S. Wang, C.Y. Tsai, C.G. Chao, T.F. Liu, Mater. Chem. Phys. 114 (2009) 595.
13. S.C. Chang, W.H. Weng, H.C. Chen, S.J. Lin, P.C.K. Chung, Wear 181-183 (1995) 511.
14. C.J. Wang, Y.C. Chang, Mater. Chem. Phys. 76 (2002) 151.
15. J.G. Duh, C.J. Wang, J. Mater. Sci. 25 (1990) 268.
16. Y.H. Tuan, C.L. Lin, C.G. Chao, T.F. Liu, Mater. Trans. 49 No.7 (2008) 1589.

- 17.C.M. Liu, H.C. Cheng, C.Y. Chao, K.L. Ou, *J. Alloys and Comp.* 488 (2009) 52.
- 18.J.W. Edington, *Practical Electron Microscopy in Materials Science*, Van Nostrand Reinhold Company, New York, 1976.
- 19.F. Ernst, Y. Cao, G.M. Michal, *Acta Mater.* 52 (2004) 1469.
- 20.H.I. Faraoun, Y.D. Zhang, C. Esling, H. Aourag, *J. App. Phys.* 99 (2006) 093508.
- 21.E. Bauer-Grosse, C. Frantz, G. Lecaer, *J. Non-Crys. Solids* 44 (1981) 277.
- 22.V.D. Blank, Y.L. Alshevskiy, A.I. Zaitsev, N.V. Kazennov, I.A. Perezhagin, B.A. Kulnitskiy, *Scripta Mater.* 55 (2006) 1035.
- 23.M. Audier, P. Bowen, W. Jones, *J. Crys. Growth* 64 (1983) 291.
- 24.X. Huang, N.H. Pryds, *Acta Mater.* 48 (2000) 4073.

# **Chapter 5.**

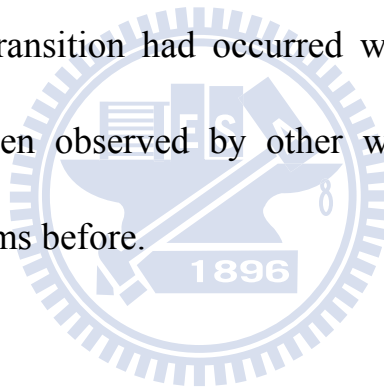
## **Phase transformations in an Fe-30Mn-10Al-4Cr-0.45C alloy**



# Phase transformations in an Fe-30Mn-10Al-4Cr-0.45C alloy

## Abstract

The as-quenched microstructure of the Fe-30wt.%Mn-10wt.%Al-4wt.%Cr-0.45wt.%C alloy was ( $\alpha + \gamma$ ) dual phases. When the as-quenched alloy was aged at 650°C, fine  $\kappa'$  carbides were formed within the  $\gamma$  grains. Additionally, a (B2 + Hägg carbide)  $\rightarrow$  (B2 + Hägg carbide +  $\beta$ -Mn)  $\rightarrow$  (B2 + Hägg carbide +  $\beta$ -Mn +  $M_{23}C_6$  carbide) phase transition had occurred within the  $\alpha$  grain. This phase transition has never been observed by other workers in the FeMnAlC and FeMnAlCrC alloy systems before.





## 5-1 Introduction

The microstructural developments of the Fe-(23-34)wt.%Mn-(5.3-11) wt.%Al-(0.4-1.3)wt.%C alloys have been extensively studied by many workers [1-9]. In these studies, it is seen that the as-quenched microstructure of the FeMnAlC alloys with  $0.54 \leq C \leq 1.3$  wt.% was single-phase austenite ( $\gamma$ ) [1-6]. When the alloys were aged at 500-750°C for moderate times, fine and coarse (Fe,Mn)<sub>3</sub>AlC carbide having an L'1<sub>2</sub>-type structure could be observed to precipitate coherently within the  $\gamma$  matrix and heterogeneously on the  $\gamma/\gamma$  grain boundaries, respectively [1-6]. For convenience, the  $\kappa'$  carbide and  $\kappa$  carbide were used to represent the (Fe,Mn)<sub>3</sub>AlC carbide formed coherently within the  $\gamma$  matrix and heterogeneously on the  $\gamma/\gamma$  grain boundaries [2]. After prolonged aging time within this temperature range, the coarse  $\kappa$  carbide would grow into adjacent  $\gamma$  grains through a  $\gamma \rightarrow \alpha$  (ferrite) +  $\beta$ -Mn reaction, a  $\gamma \rightarrow \gamma_0$  (carbon-deficient austenite) +  $\kappa$  reaction, a  $\gamma \rightarrow \beta$ -Mn +  $\kappa$  reaction or a  $\gamma \rightarrow \alpha$  +  $\beta$ -Mn +  $\kappa$  reaction on the grain boundaries in the fully austenitic FeMnAlC alloys, depending on the chemical composition and aging temperature [1-5]. In contrast to the alloys with  $0.54 \leq C \leq 1.3$  wt.%, the as-quenched microstructure of the FeMnAlC alloys with  $0.4 \leq C \leq 0.51$  wt.% was ( $\alpha + \gamma$ ) dual phases [7-9]. When the alloys were aged at 550-710°C for moderate times, fine  $\kappa'$  carbides were found to precipitate within the  $\gamma$  matrix, and coarse  $\kappa$  carbides as well as

$\beta$ -Mn precipitates could be observed within the  $\alpha$  grains and on the  $\alpha/\alpha$  grain boundaries [8, 9]. In 1991, the present workers examined the microstructural developments of an Fe-28.6wt.%Mn-10.1wt.%Al-0.46wt.%C alloy [10]. Consequently, it was found that in the as-quenched condition, extremely fine  $D0_3$  domains could be observed within the  $\alpha$  grains. This is different from that reported by other workers in the  $(\alpha + \gamma)$  duplex FeMnAlC alloys [7-9]. When the alloy was aged at temperatures ranging from 450°C to 750°C, the phase transformation sequence occurring within the  $\alpha$  grain was found to be  $\alpha + D0_3 \rightarrow \alpha + D0_3 + \kappa \rightarrow \alpha + B2 + \kappa \rightarrow \alpha$  [10].

In order to improve the corrosion resistance, the Cr has been added to the fully austenitic FeMnAlC alloys [11-15]. Based on these studies, it can be generally concluded that the addition of Cr does achieve the result. Additionally, the effects of Cr addition on the microstructures of the FeMnAlC alloys have also been examined by several researchers [16-17]. In the previous study [16], it is seen that when the austenitic Fe-30wt.%Mn-9wt.%Al-5wt.%Cr-0.7wt.%C alloy was aged at 550-750°C, the fine  $\kappa'$  carbides were formed within the  $\gamma$  grain, and a  $(M_7C_3 + D0_3) \rightarrow (M_7C_3 + B2) \rightarrow (M_7C_3 + \alpha)$  reaction occurred on the  $\gamma/\gamma$  grain boundaries. Besides, when the austenitic Fe-28.3wt.%Mn-8.7wt.%Al-5.5wt.%Cr-1wt.%C alloy was aged at 800-1250°C, a  $(\gamma + Cr_7C_3) \rightarrow \gamma \rightarrow (\gamma + (\alpha + B2 + D0_3))$  reaction occurred within the  $\gamma$  grain and on the  $\gamma/\gamma$  grain

boundaries [17]. However, little information concerning the microstructural developments of the ( $\alpha + \gamma$ ) duplex FeMnAlCrC alloys has been provided in the literatures. Recently, the present workers have examined the microstructural developments of a ( $\alpha + \gamma$ ) duplex Fe-30wt.%Mn-10wt.%Al-4wt.%Cr-0.45wt.%C alloy [18]. Consequently, it was found that when the alloy was aged at 550°C, the fine  $\kappa'$  carbides were formed within the  $\gamma$  grain and Hägg carbides ( $M_5C_2$ -type carbides) occurred at the  $a/2\langle 100 \rangle$  anti-phase boundaries of the well-grown  $D0_3$  domains. The Hägg carbide has a monoclinic structure with lattice parameters  $a=1.158\text{nm}$ ,  $b=0.452\text{nm}$ ,  $c=0.509\text{nm}$ , and  $\beta=98.3^\circ$ . The orientation relationship between the Hägg carbide and  $D0_3$  matrix was determined to be  $(\bar{5}10)_{M_5C_2} // (1\bar{1}0)_{D0_3}$  and  $(134)_{M_5C_2} // (10\bar{2})_{D0_3}$ . It is noted that the Hägg carbide has never been observed by other workers in the FeMnAlC and FeMnAlCrC alloy systems before. Additionally, the orientation relationship between Hägg carbide and bcc-type phase has also never been reported by other workers. Extending the previous work, the purpose of this study is an attempt to examine the microstructural evolution of the Fe-30wt.%Mn-10wt.%Al-4wt.%Cr-0.45wt.%C alloy aged at 650°C.

## **5-2 Experimental procedure**

The Fe-30wt.%Mn-10wt.%Al-4wt.%Cr-0.45wt.%C alloy was prepared in a vacuum induction furnace by using pure Fe, Mn, Al, Cr and carbon powder under a protective argon atmosphere. After being homogenized at 1250°C for 12 h, the ingot was hot-rolled and then cold-rolled to a final thickness of 2.0 mm. The sheets were subsequently solution heat-treated (SHT) at 1050°C for 1 h and then quenched into room-temperature water rapidly. Aging processes were performed at 650°C for various times in a vacuum heat-treated furnace followed by rapid quenching. Electron microscopy specimens were prepared by means of a double-jet electropolisher with an electrolyte of 65% ethanol, 20% acetic acid and 15% perchloric acid. Electron microscopy was performed on JEOL-2100 transmission electron microscope (TEM) operating at 200kV. This microscope was equipped with a Link ISIS 300 energy-dispersive X-ray spectrometer (EDS) for chemical analysis. Quantitative analyses of elemental concentrations for Fe, Mn, Al and Cr were made using the Cliff-Lorimer ratio thin section method. The EDS with a thick-window detector is limited to detect the elements of atomic number of 11 or above. Therefore, carbon cannot be examined by this method.

### **5-3 Results and discussion**

In the as-quenched condition, the microstructure of the alloy was ( $\alpha + \gamma$ ) dual phases and no precipitates could be detected within the  $\gamma$  grains. Figure 5.1(a) is a selected-area diffraction pattern (SADP) taken from the  $\alpha$  grain, exhibiting the presence of the superlattice reflection spots of the ordered  $D0_3$  phase [19]. Figures 5.1(b) and (c) are (111) and (200)  $D0_3$  dark-field (DF) electron micrographs, clearly showing the presence of extremely fine  $D0_3$  domains and small B2 domains, respectively. The extremely fine  $D0_3$  domains were formed within the  $\alpha$  grain by a  $\alpha \rightarrow B2 \rightarrow D0_3$  continuous ordering transition during quenching [19]. This is similar to that observed by the present workers in the Fe-28.6wt.%Mn-10.1wt.%Al-0.46wt.%C alloy [10]. When the as-quenched alloy was aged at 650°C for 6 h, fine  $k'$  carbides were formed within the  $\gamma$  grains, as shown in Figure 5.2(a). Figure 5.2(b) is a bright-field (BF) electron micrograph taken from the  $\alpha$  grain, indicating that some precipitates started to appear within the  $\alpha$  grain. Figures 5.2 (c) and (d) are (111) and (200)  $D0_3$  DF electron micrographs, indicating that the B2 domains grew significantly and the  $D0_3$  domains remained to be extremely fine. Apparently, the B2 phase existed at the aging temperature and the extremely fine  $D0_3$  domains were formed by a  $B2 \rightarrow D0_3$  ordering transition during quenching [19]. Figures 5.3(a) through (c) are three SADPs taken from the precipitate marked as “C” in Figure

5.2(b). According to the camera length and the measurement of angles as well as d-spacings of the diffraction spots, the crystal structure of the precipitate phase was determined to be monoclinic with lattice parameters  $a=1.158$  nm,  $b=0.452$  nm,  $c=0.509$  nm, and  $\beta=98.3^\circ$ , which corresponds to that of the Hägg carbide [18, 20-24]. It is clear that when the alloy was aged at  $650^\circ\text{C}$  for 6 h, the microstructure within the  $\alpha$  grain was a mixture of (B2 + Hägg carbide). When the aging time was increased to 12 h, a new phase was found to occur on the  $\alpha/\alpha$  grain boundaries, as shown in Figure 5.4(a). Figure 5.4(b) is a SADP taken from the phase marked as “B” in Figure 5.4(a), indicating that the new phase on the  $\alpha/\alpha$  grain boundaries is  $\beta$ -Mn having a simple cubic structure with lattice parameter  $a=0.632$  nm [25]. Figures 5.4(c) through (e) are three SADPs taken from the  $\beta$ -Mn marked as “B” and its surrounding B2 matrix, indicating that the orientation relationship between  $\beta$ -Mn and B2 phase was  $(100)_{\text{B2}} // (100)_{\beta\text{-Mn}}$ ,  $(010)_{\text{B2}} // (02\bar{1})_{\beta\text{-Mn}}$ ,  $(01\bar{1})_{\text{B2}} // (01\bar{3})_{\beta\text{-Mn}}$ , which is similar to that observed by the present workers in the Fe-29.9wt.%Mn-9.1wt.%Al-2.9wt.%Cr alloy [25]. When the aging time was increased to 18 h, the  $\beta$ -Mn would grow into adjacent B2 matrix, as illustrated in Figure 5.5(a). In Figure 5.5(a), it is also seen that another precipitate started to appear within the  $\beta$ -Mn region. Figure 5.5(b) is a BF electron micrograph taken from an area containing the precipitate and its surrounding  $\beta$ -Mn. Figures 5.5(c) through (e) are three SADPs taken from the

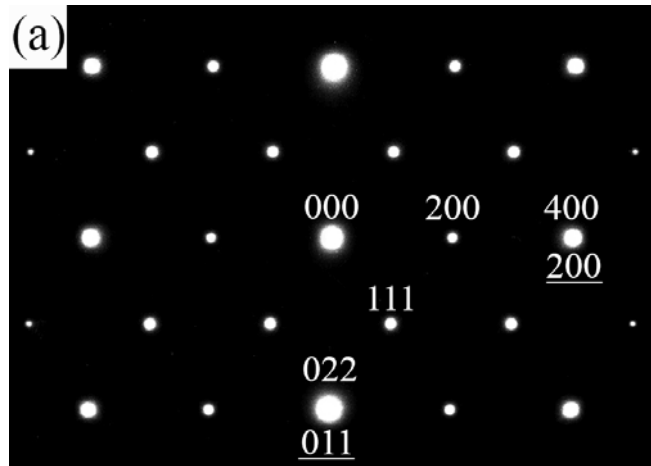


Figure 5.1 (a)

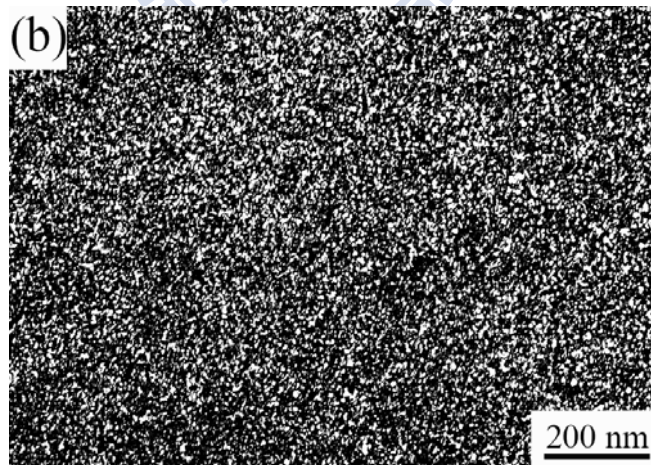


Figure 5.1 (b)

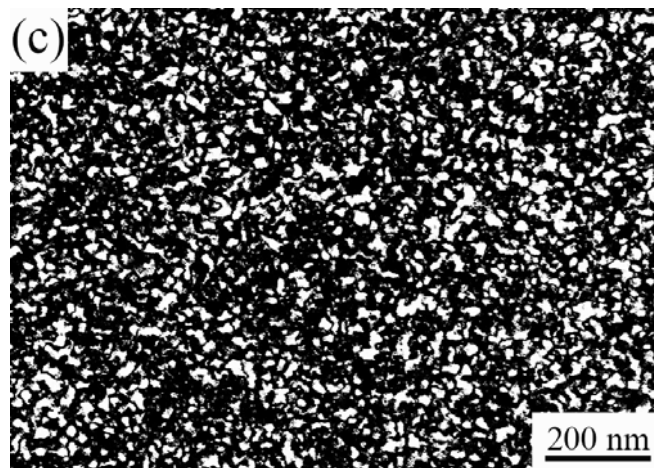


Figure 5.1 (c)

Figure 5.1 Transmission electron micrographs of the as-quenched alloy. (a) an SADP taken from the  $\alpha$  grain. The zone axis is  $[01\bar{1}]$  (hkl:  $\alpha$  phase, hkl:  $D0_3$  phase). (b) and (c) (111) and (200)  $D0_3$  DF images, respectively.



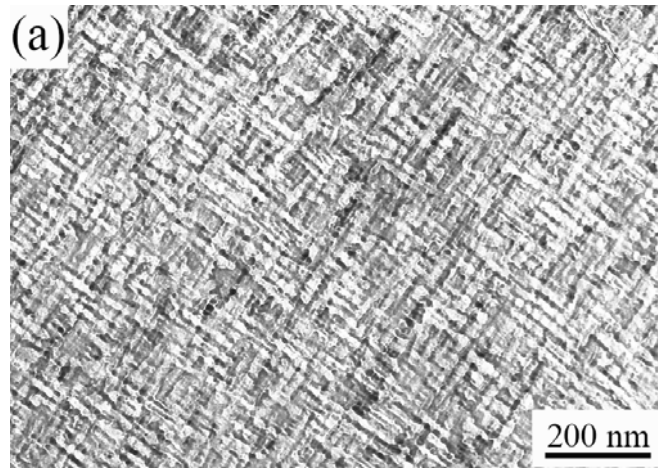


Figure 5.2 (a)

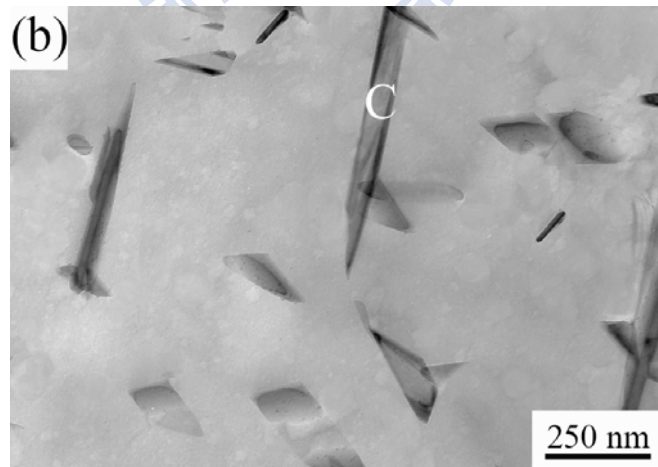


Figure 5.2 (b)

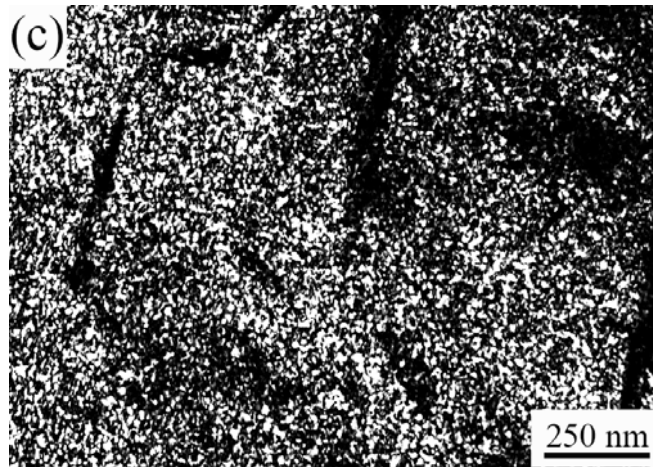


Figure 5.2 (c)

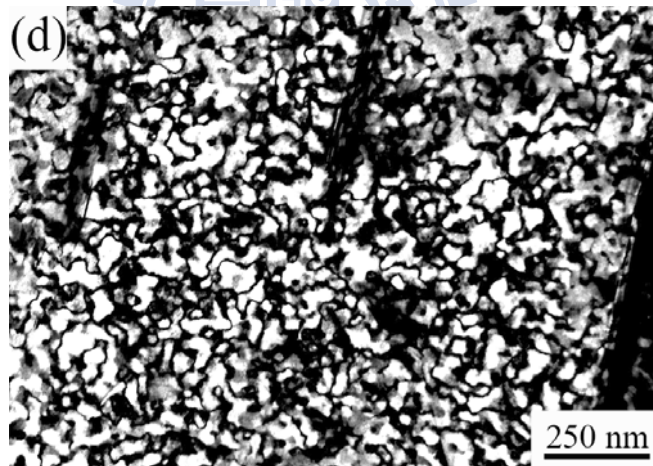


Figure 5.2 (d)

Figure 5.2 Transmission electron micrographs of the alloy aged at 650°C for 6 h. (a) BF taken from the  $\gamma$  grain. (b) BF taken from the  $\alpha$  grain. (c) and (d) (111) and (200)  $D0_3$  DF images, respectively.

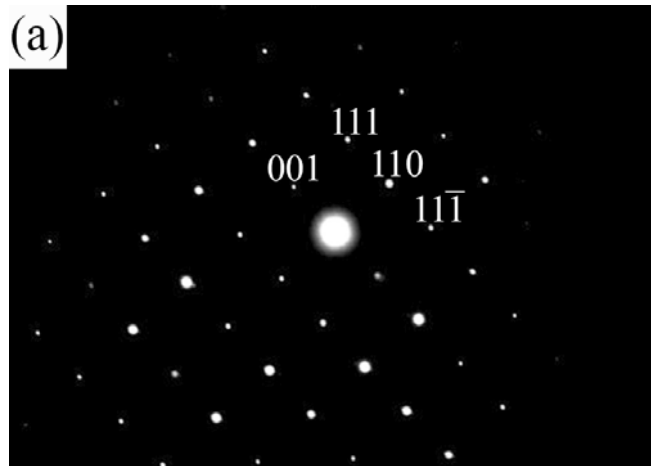


Figure 5.3 (a)



Figure 5.3 (b)

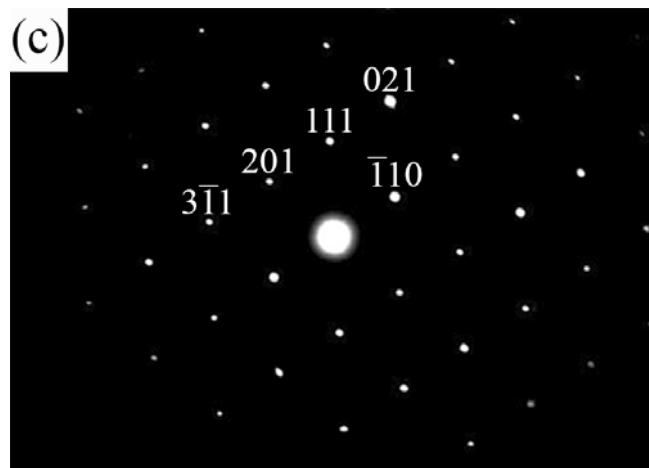


Figure 5.3 (c)

Figure 5.3 (a) through (c) Three SAPDs taken from the precipitate marked “C” in Figure 5.2(b). The zone axes are (a)  $[1\bar{1}0]$ , (b)  $[10\bar{1}]$  and (c)  $[11\bar{2}]$ , respectively.

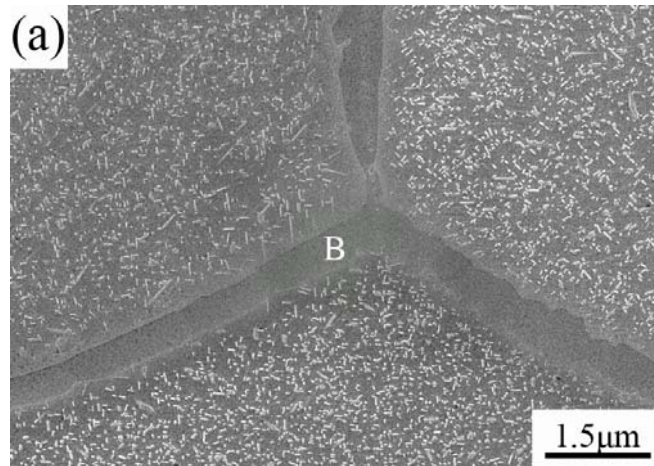


Figure 5.4 (a)

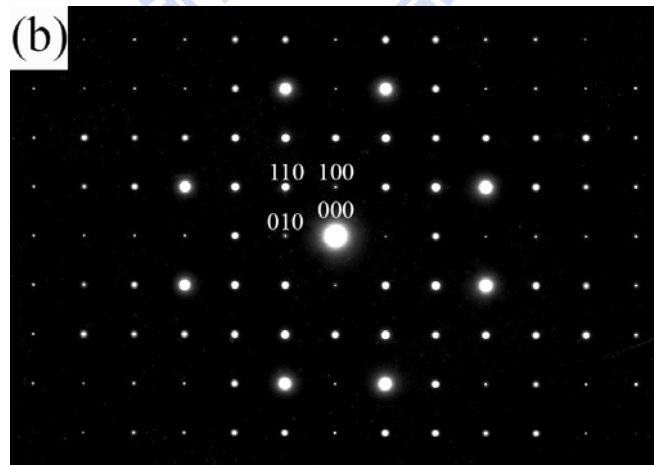


Figure 5.4 (b)

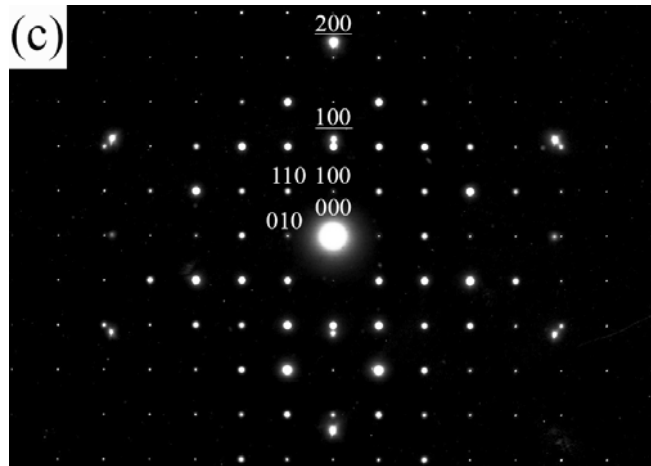


Figure 5.4 (c)

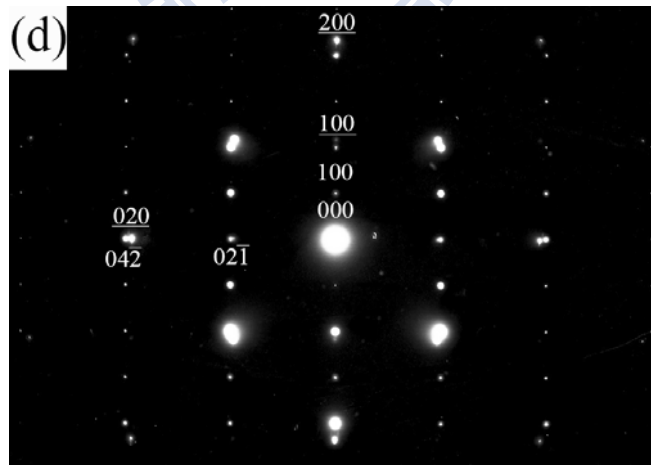


Figure 5.4 (d)

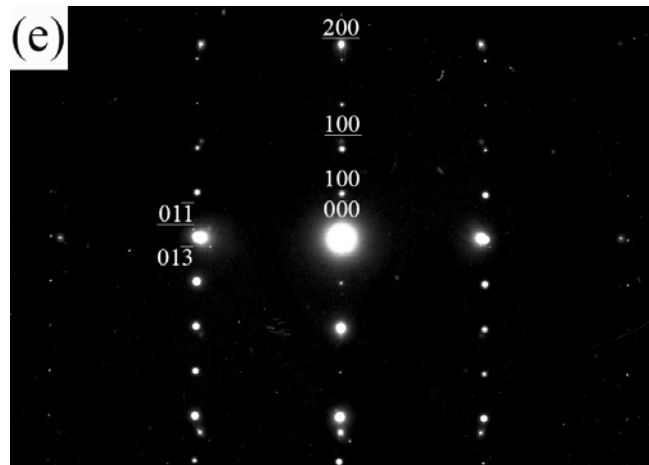


Figure 5.4 (e)

Figure 5.4 (a) SEM image of the alloy aged at 650°C for 12 h. (b) an SADP taken from the precipitate marked “B” in Figure 5.4(a). The zone axis is [001]. (c) through (d) Three SADPs taken from an area including the precipitate marked “B” in Figure 5.4(a) and its surrounding matrix. The zone axes are (c)  $[001]_{\beta\text{-Mn}}$ ,  $[0\bar{1}2]_{\text{B}_2}$ , (d)  $[012]_{\beta\text{-Mn}}$ ,  $[001]_{\text{B}_2}$  and (e)  $[031]_{\beta\text{-Mn}}$ ,  $[011]_{\text{B}_2}$ , respectively.

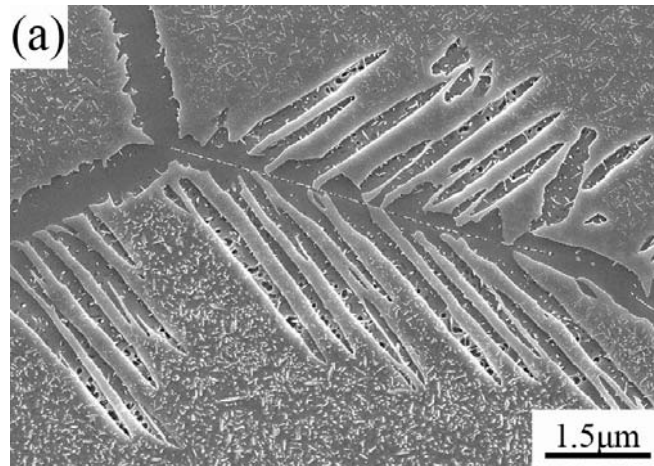


Figure 5.5 (a)

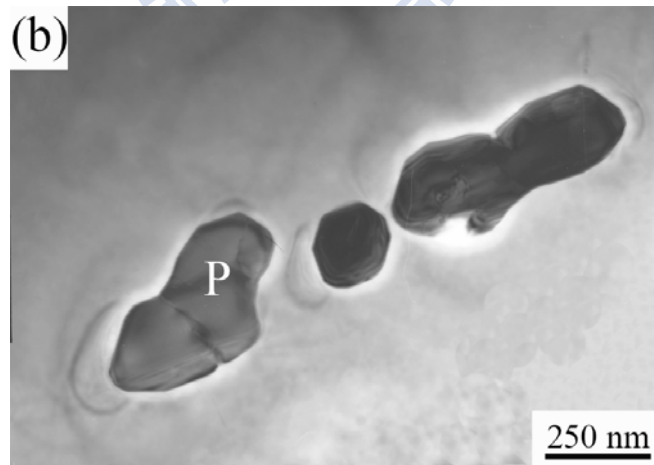


Figure 5.5 (b)



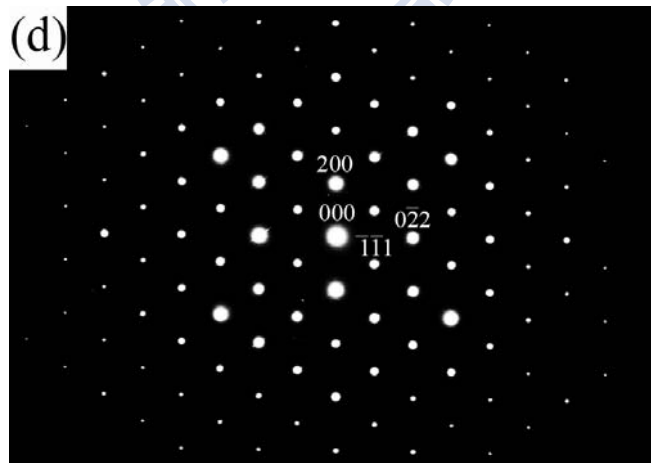
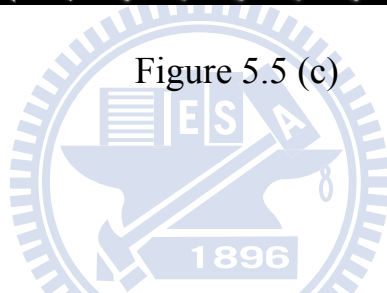
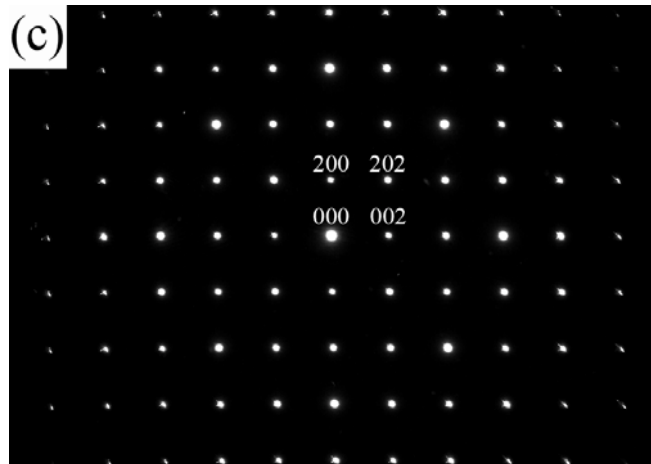


Figure 5.5 (d)

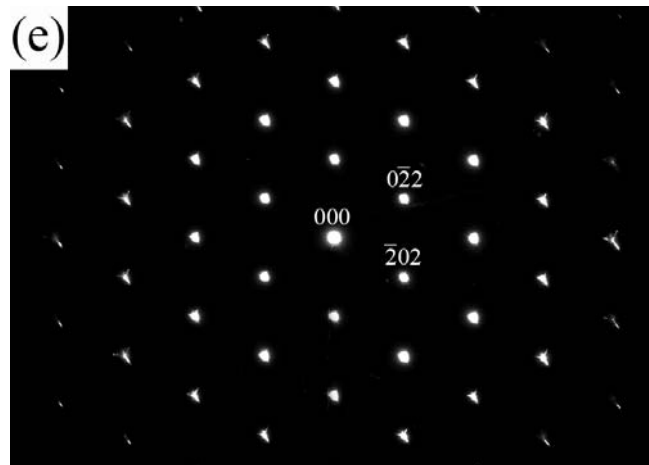


Figure 5.5 (e)

Figure 5.5 (a) SEM image of the alloy aged at 650°C for 18 h. (b) through (e) Transmission electron micrographs of the alloy aged at 650°C for 18 h. (b) BF. (c) through (e) Three SADPs taken from the precipitate marked “P” in Figure 5.5(b). The zone axes are (c) [010], (d) [011] and (e) [111], respectively.

precipitate marked as “P” in Figure 5.5(b), indicating that the precipitate was  $M_{23}C_6$ -type carbide having a face-centered cubic (f.c.c) structure with lattice parameter  $a=1.079$  nm [26]. After further prolonged aging, the  $\beta$ -Mn occurred to form inside the B2 matrix with different variants, as shown in Figure 5.6.

Based on the preceding results, some discussion is appropriate. That the phase transition  $(B2 + \text{Hägg carbide}) \rightarrow (B2 + \text{Hägg carbide} + \beta\text{-Mn}) \rightarrow (B2 + \text{Hägg carbide} + \beta\text{-Mn} + M_{23}C_6 \text{ carbide})$  occurred in the alloy aged at  $650^\circ\text{C}$  is a remarkable feature in the present study. In order to clarify this feature, an TEM-EDS study was made. The chemical compositions of the Hägg carbide,  $M_{23}C_6$  carbide,  $\beta$ -Mn and B2 phase in the alloy aged at  $650^\circ\text{C}$  for different times are listed in Table 5.1. In the Fe-Al phase diagram [19], it is seen that when the Fe-Al alloy with  $\text{Al} \geq 25.1$  at.% is heat-treated at  $650^\circ\text{C}$  and then quenched to room-temperature, the microstructure present at  $650^\circ\text{C}$  was B2 phase and a  $B2 \rightarrow D0_3$  ordering transition would occur during quenching. The Al content of the B2 domain after being aged at  $650^\circ\text{C}$  for 6 h is 25.28 at.%, as seen in Table 5.1. Therefore, it is reasonable to suggest that the microstructure of the matrix at  $650^\circ\text{C}$  would be the B2 phase and extremely fine  $D0_3$  domains were formed by a  $B2 \rightarrow D0_3$  ordering transition during quenching, which is similar to that seen in the Fe-Al binary alloys. It is also seen in Table 5.1 that the Mn and Cr contents

of the B2 domain in the alloy aged at 650°C for 6 h are much lower than those of the  $\alpha$  phase in the as-quenched alloy, suggesting that the surrounding region would be enriched in Mn and Cr due to the growth of the B2 domains. It is reasonable to believe that the enrichment of Mn and Cr contents would enhance the formation of the (Mn,Cr)-rich Hägg carbide at the region contiguous to the B2 domains. Consequently, when the as-quenched alloy was aged at 650°C for 6 h, the microstructure was a mixture of (B2 + Hägg carbide). After prolonged the aging time to 12 h, the  $\beta$ -Mn preferred to form heterogeneously on the  $\alpha/\alpha$  grain boundaries, which is similar to that observed in the FeMnAlCr alloys in the previous study [25]. In the Fe-Mn binary alloy, the  $\beta$ -Mn could only be found at temperature above 707°C with Mn  $\geq$  70 at.% [27]. However, the addition of Al would cause the  $\beta$ -Mn region to extend considerably [25]. Additionally, due to the formation of Mn-rich  $\beta$ -Mn, the (Mn,Cr)-rich Hägg carbide was observed to be disappeared within the  $\beta$ -Mn phase. Therefore, the microstructure of the aged at 650°C for 12 h was a mixture of (B2 + Hägg carbide +  $\beta$ -Mn). Furthermore, when the aging time was increased to 18 h, the  $M_{23}C_6$  carbides started to form within the  $\beta$ -Mn phase. Since the  $\beta$ -Mn has a simple cubic structure, the solubility of C could be expected to be low. Besides, it is well known that the Cr atom is a strong carbide former. In Table 5.1, it is clearly seen that the Cr content in the B2 phase in the alloy aged for 18 h were slightly less than that in

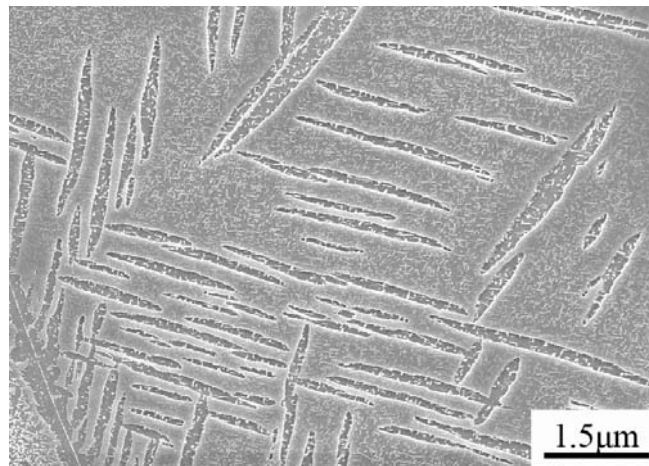


Figure 5.6

Figure 5.6 SEM image of the alloy aged at 650°C for 36 h.

Table 5.1 Chemical compositions of the phases revealed by energy-dispersive X-ray spectrometer (EDS).

Heat Treatment	Phase	Chemical Compositions (at.%)			
		Fe	Mn	Al	Cr
SHT	$\gamma$	48.90	30.26	17.13	3.71
	$\alpha$	52.24	21.67	21.52	4.57
650°C, 6 h	B2	57.26	16.49	25.28	0.97
	$M_5C_2$	29.60	44.39	1.12	24.89
650°C, 12 h	B2	59.88	13.93	25.32	0.87
	$M_5C_2$	30.69	43.21	1.08	25.02
	$\beta$ -Mn	41.29	36.64	16.58	5.49
650°C, 18 h	B2	59.67	14.22	25.26	0.85
	$M_5C_2$	31.63	42.36	1.05	24.96
	$\beta$ -Mn	41.42	37.54	17.41	3.63
	$M_{23}C_6$	53.67	21.62	0.87	23.84

the alloy aged for 12 h. Therefore, the reason why  $M_{23}C_6$  carbide occurred to form within the  $\beta$ -Mn phase is plausible that the C content was expected to be supersaturated and the Cr atom preferred to form a carbide phase as  $M_{23}C_6$  rather than fully dissolve in the  $\beta$ -Mn phase. Consequently, the microstructure of the alloy aged at  $650^\circ\text{C}$  for longer than 18 h was a mixture of (B2 + Hägg carbide +  $\beta$ -Mn +  $M_{23}C_6$  carbide).

Finally, it is worthwhile pointing out that the presence of the  $M_{23}C_6$  carbides within the  $\beta$ -Mn phase has never been observed by other workers before. The orientation relationship between the  $M_{23}C_6$  carbide and the  $\beta$ -Mn phase has also not been reported in the FeMnAlC or FeMnAlCrC alloy systems in the previous literatures. Obviously, in order to clarify the orientation relationship between the  $M_{23}C_6$  carbide and  $\beta$ -Mn phase, a further work is needed.

## **5-4 Conclusions**

The as-quenched microstructure of the Fe-30wt.%Mn-10wt.%Al-4wt.%Cr-0.45wt.%C alloy was ( $\alpha + \gamma$ ) dual phases. No precipitates could be detected within the  $\gamma$  grains, whereas extremely fine  $D0_3$  domains could be observed within the  $\alpha$  grains. The extremely fine  $D0_3$  domains were formed by a  $\alpha \rightarrow B2 \rightarrow D0_3$  continuous ordering transition during quenching. When the as-quenched alloy was aged at  $650^\circ\text{C}$ , fine  $\kappa'$  carbides were precipitated within the  $\gamma$  grains. Additionally, with increasing the aging time at  $650^\circ\text{C}$ , a ( $B2 + \text{Hägg carbide}$ )  $\rightarrow$  ( $B2 + \text{Hägg carbide} + \beta\text{-Mn}$ )  $\rightarrow$  ( $B2 + \text{Hägg carbide} + \beta\text{-Mn} + M_{23}C_6$  carbide) phase transition had occurred within the  $\alpha$  grains. This phase transition has never been observed by other workers in the FeMnAlC and FeMnAlCrC alloy systems before.



## References

1. K. Sato, K. Tagawa, Y. Inoue, Metall. Trans. A 21A (1990) 5.
2. W.K. Choo, J.H. Kim, J.C. Yoon, Acta Mater. 45 No.12 (1997) 4877.
3. C.Y. Chao, C.N. Hwang, T.F. Liu, Scripta Metall. 28 (1993) 109.
4. G.S. Krivonogov, M.F. Alekseyenko, G.G. Solovyeva, Fiz. Metal. Metalloved 39 No.4 (1975) 775.
5. C.N. Hwang, C.Y. Chao, T.F. Liu, Scripta Metall. 28 (1993) 263.
6. T.F. Liu, J.S. Chou, C.C. Wu, Metall. Trans. A 21A (1990) 1891.
7. S.C. Tjong, S.M. Zhu, Mater. Trans. 38 No.2 (1997) 112.
8. S.C. Tjong, N.J. Ho, Metallography 21 (1988) 199.
9. T.F. Liu, C.M. Wan, Strength Met. Alloys 1 (1986) 423.
10. C.C. Wu, J.S. Chou, T.F. Liu, Metall. Trans. A 22A (1991) 2265.
11. C.S. Wang, C.Y. Tsai, C.G. Chao, T.F. Liu, Mater. Trans. 48 (2007) 2973.
12. Y.H. Tuan, C.S. Wang, C.Y. Tsai, C.G. Chao, T.F. Liu, Mater. Chem. Phys. 114 (2009) 595.
13. S.C. Chang, W.H. Weng, H.C. Chen, S.J. Lin, P.C.K. Chung, Wear 181-183 (1995) 511.
14. C.J. Wang, Y.C. Chang, Mater. Chem. Phys. 76 (2002) 151.
15. J.G. Duh, C.J. Wang, J. Mater. Sci. 25 (1990) 268.
16. Y.H. Tuan, C.L. Lin, C.G. Chao, T.F. Liu, Mater. Trans. 49 No.7 (2008)

- 1589.
17. C.M. Liu, H.C. Cheng, C.Y. Chao, K.L. Ou, *J. Alloys and Comp.* 488 (2009) 52.
  18. Y.H. Tuan, C.G. Chao, T.F. Liu, *Mater. Trans.* 51 No.6 (2010) 1168.
  19. S.M. Allen, J.W. Cahn, *Acta Metall.* 24 (1976) 425.
  20. F. Ernst, Y. Cao, G.M. Michal, *Acta Mater.* 52 (2004) 1469.
  21. H.I. Faraoun, Y.D. Zhang, C. Esling, H. Aourag, *J. App. Phys.* 99 (2006) 093508.
  22. E. Bauer-Grosse, C. Frantz, G. Lecaer, *J. Non-Crys. Solids* 44 (1981) 277.
  23. V.D. Blank, Y.L. Alshevskiy, A.I. Zaitsev, N.V. Kazennov, I.A. Perezhugin, B.A. Kulnitskiy, *Scripta Mater.* 55 (2006) 1035.
  24. M. Audier, P. Bowen, W. Jones, *J. Crys. Growth* 64 (1983) 291.
  25. T.F. Liu, C.C. Wu, *Scripta* 23 (1989) 1087.
  26. T.F. Liu, S.W. Peng, Y.L. Lin C.C. Wu, *Metall. Trans. A* 21 (1990) 567.
  27. V.G. Rivlin, *Inter. Metals Review* 28 No.6 (1983) 309.

## List of Publications

### ● Journal Papers

1. Y.H. Tuan, C.L. Lin, C.G. Chao and T.F. Liu, “Grain Boundary Precipitation in Fe-30Mn-9Al-5Cr-0.7C Alloy”, Mater. Trans. JIM 49 No.7 (2008) 1589-1593.
2. Y.H. Tuan, C.S. Wang, C.Y. Tsai, C.G. Chao and T.F. Liu, “Corrosion behaviors of austenitic Fe-30Mn-7Al-xCr-1C alloys in 3.5% NaCl solution”, Mater. Chem. and Phys. 114 (2009) 595-598.
3. Y.H. Tuan, C.G. Chao and T.F. Liu, “Formation of Hägg Carbide in an Fe-30Mn-10Al-4Cr-0.45C Alloy”, Mater. Trans. JIM 51 No.6 (2010) 1168-1172.
4. Y.H. Tuan, C.G. Chao and T.F. Liu, “Phase transformations in an Fe-30Mn-10Al-4Cr-0.45C alloy”, submitted to J. Alloy. Compd.
5. G.D. Tsay, C.W. Su, Y.H. Tuan, C.G. Chao and T.F. Liu, “Phase separation from  $L2_1$  to  $(B2+L2_1)$  in Fe-24.6Al-7.5Ti alloy”, Accepted and to be published in Mater. Trans. JIM. (2010,7)
6. G.D. Tsay, Y.H. Tuan, C.L. Lin, C.G. Chao and T.F. Liu, " Effect of Carbon Content on Spinodal Decomposition in Fe-26at.%Mn-20at.%Al-yat.%C Alloys”, submitted to Mater. Trans. JIM.

● **Conferences Papers**

1. 張凱明, 劉亮延, 林志龍, 段逸軒, 蔡國棟, 陳柏至, 王浩仰, 薄慧雲, 劉增豐, 朝春光, “鐵-9 鋁-30 錳-2 碳合金之顯微結構與機械性質”, Proceedings of The 2009 Annual Conference of The Chinese Society for Materials Science (2009).
2. Y.H. Tuan, P.C. Chen, S.Y. Su, X.L. Lin, Z.L. Lin, C.S. Wang, C.G. Chao, T.F. Liu, "Grain boundary precipitation in Fe-30Mn-9Al-5Cr-0.7C alloy", Proceedings of The 2008 Annual Conference of The Chinese Society for Materials Science (2008).
3. 李堅瑋, 蘇俊瑋, 段逸軒, 劉增豐 "熱浸鍍鋁鐵鋁錳碳合金之研究", Proceedings of The 2003 Annual Conference of The Chinese Society for Materials Science OA-006, (2003).
4. J.W. Lee, Y.H. Tuan, C.S. Wang and T.F. Liu, "Phase Transformations in Fe-9.02Al-30.0Mn-4.0Cr Alloy", Proceedings of The 2002 Annual Conference of The Chinese Society for Materials Science, A-4, (2002).
5. J.W. Lee, C.S. Wang, Y.H. Tuan, J.S. Lin and T.F. Liu, "Phase Transformations in an Fe-7.5Al-7Ni-1.4C Alloy", Proceedings of The 2001 Annual Conference of The Chinese Society for Materials Science, A-26, (2001).